Title

Integration and calibration of UBCSAND model for drained monotonic and cyclic triaxial compression of aggregates

Permalink

https://escholarship.org/uc/item/7bk4j99m

Authors

Voyagaki, Elia
Kishida, Tadahiro
Aldulaimi, Rusul Falah
et al.

Publication Date

2023-08-01

DOI

10.1016/j.soildyn.2023.107978

Peer reviewed
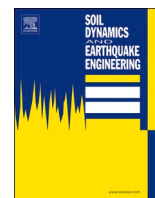
Integration and calibration of UBCSAND model for drained monotonic and cyclic triaxial compression of aggregates

Elia Voyagaki [a,b], Tadahiro Kishida [a], Rusul Falah Aldulaimi [a], George Mylonakis [a,b,*]

[a] *Khalifa University of Science & Technology, Abu Dhabi, United Arab Emirates*
[b] *University of Bristol, Bristol, UK*

A B S T R A C T

We report on results from triaxial drained monotonic and cyclic compression tests for four different aggregates (gabbro, limestone, demolished concrete, steel slag), and discuss the applicability of UBCSAND model for simulating the relevant non-linear stress-strain curves. First, UBCSAND is integrated analytically for the elastic and plastic volumetric and deviatoric strains, leading to a pair of novel closed-form solutions expressed in terms of hypergeometric functions. These solutions are inherently free of numerical errors and can be used for the evaluation of results from numerical integration. Second, three calibration techniques for the model parameters are presented and compared: (1) a graphical "chart" solution based on results from forward numerical simulations; (2) a numerical approach based on minimization of residuals; and (3) an informed trial-and-error approach based on the analytical solution. Errors in numerical integration of the model are explored by comparing the analytical solution against results from an Euler integration. Variations in the calibrated parameters are discussed for drained monotonic and cyclic triaxial loading considering different types of aggregates.

1. Introduction

Understanding drained monotonic and cyclic behavior of ballast aggregates is key in railway foundation design. The UBCSAND model [1–3] is often employed in such analyses, as a simple alternative to more complex constitutive formulations for predicting monotonic and cyclic response of granular soil under drained and undrained conditions [4–23]. The specific model is employed in commercial finite difference and finite element software (e.g. Refs. [3,24–26]) as it realistically simulates volumetric and deviatoric strains in granular soils under monotonic and cyclic loading. The model has been applied to liquefaction studies [27] and can be modified to capture stiffness degradation upon liquefaction due to fabric evolution [28]. Under drained conditions, however, the evolution of soil fabric is limited until the volumetric response starts exhibiting dilatant behavior [29], so relevant adjustments for stiffness degradation would not be required as long as the material remains in the contractive regime.

Calibration procedures of the UBCSAND model parameters for undrained conditions are available (e.g. Refs. [30–34]). Elastic moduli can be determined from measured or estimated shear wave propagation velocities (V_s) and other procedures [31]. While wave methods provide the most rational means for establishing elastic moduli, some researchers (e.g., Li et al. [35]) suggest that elastic moduli may be selected from isotropic compression data or the initial slope of the stress-strain curves from drained triaxial compression data, when the plastic potential surface follows similar patterns as the UBCSAND. As the initial slope of monotonic compression tests can underestimate the elastic moduli for cyclic loading, the aforementioned alternative approaches should be used with caution as their validity depends of the strain level of interest. Beaty [31] recommends that the stress ratios at failure (η_f) and constant volume (η_{cv}) can be selected by considering the interaction between the two parameters. These are established by simulating cyclic-loading response over the effective stress range of interest, especially in terms of cyclic resistance ratio, accumulation of strain, and post-liquefaction stiffness. These approaches determine the model parameters related to plastic deformations following the selection of elastic properties at low strains. A calibration procedure of the UBCSAND model for drained response is described in Ref. [32]. The specific calibration can reproduce available shear modulus reduction (G/G_o) and equivalent damping ratio values (ξ) as a function of cyclic shear strain amplitude (γ) [36–40].

The study at hand develops and compares three novel methodologies for calibrating the UBCSAND model to data from drained monotonic and

---

cyclic triaxial compression tests. To this end, an experimental campaign was carried out in the Geotechnical Materials Lab at Khalifa University on four types of aggregates: gabbro, limestone, demolished concrete and steel slag. These aggregates have different mineralogy and exhibit different material behavior under compression and shearing. UBCSAND is first integrated analytically to furnish a set of novel closed-form solutions for shear and volumetric strains. Contrary to numerical integration approaches, these solutions are free of computational errors and, thereby, can provide insight on the role of the various model parameters and their calibration against experimental data. Three calibration techniques are then developed: (1) a graphical "chart" solution based on results from forward numerical simulations; (2) a numerical approach based on minimization of residuals; (3) a trial-and-error graphical approach based on the analytical solution. These calibration procedures are applied to data from drained strain- and stress-controlled monotonic triaxial compression tests obtained by the authors. The performance of the model with number of cycles is discussed against data from cyclic compression tests.

2. Model overview

2.1. Formulation

The elastic shear and bulk moduli (G^e, K^e) can be established by means of Eqs. (1) and (2), as functions of the mean effective stress p' and Poisson's ratio ν [31]

$$G^e = k_G^e \left(\frac{p_M'}{p_a}\right)^{ne} p_a \tag{1}$$

$$K^e = \frac{2(1+\nu)}{3(1-2\nu)} G^e \tag{2}$$

where k_G^e is a dimensionless elastic shear modulus parameter, p_a is the atmospheric pressure (usually taken equal to 100 kPa) and $p_M' = (\sigma_1' + \sigma_3')/2$ is the familiar MIT mean effective stress. In Eq. (1), the elastic shear modulus exponent *ne* is often taken equal to around 0.5 based on experimental observations of small-strain shear moduli (e.g. Refs. [37,38,40]).

The incremental elastic stress-strain relation can be cast in terms of G^e and K^e as shown in Eq. (3).

$$\begin{bmatrix} dp' \\ dq \end{bmatrix} = \begin{bmatrix} K^e & 0 \\ 0 & 2G^e \end{bmatrix} \begin{bmatrix} d\varepsilon_v^e \\ d\gamma^e \end{bmatrix} \tag{3}$$

where p' and q are the corresponding Cambridge stress invariants defined as $p' = (\sigma_1' + \sigma_2' + \sigma_3')/3$, $q = \sigma_1' - \sigma_3'$ under triaxial loading, and $d\varepsilon_v^e$, $d\gamma^e$ are the corresponding incremental volumetric and shear strains $d\varepsilon_v^e = d\varepsilon_a^e + 2d\varepsilon_r^e$, $d\gamma^e = d\varepsilon_a^e - d\varepsilon_r^e$. Since UBCSAND employs the MIT stress path parameters $p_M' = \frac{1}{2}(\sigma_1' + \sigma_3')$ and $q_M = \frac{1}{2}(\sigma_1' - \sigma_3')$, Equation (3) can be recast in the following alternative forms:

$$\begin{bmatrix} dp_M' \\ dq_M \end{bmatrix} = \begin{bmatrix} K^e & G^e/3 \\ 0 & G^e \end{bmatrix} \begin{bmatrix} d\varepsilon_v^e \\ d\gamma^e \end{bmatrix} \tag{4a}$$

$$\begin{bmatrix} d\varepsilon_v^e \\ d\gamma^e \end{bmatrix} = \begin{bmatrix} 1/K^e & -1/3K^e \\ 0 & 1/G^e \end{bmatrix} \begin{bmatrix} dp_M' \\ dq_M \end{bmatrix} \tag{4b}$$

With reference to elastoplastic response, the yield surface is defined as

$$f = \eta - \eta_{mob} = 0 \tag{5}$$

where $\eta = q_M/p_M'$ is the stress ratio. Yielding occurs when η reaches the mobilized stress ratio η_{mob}. An advantage of the specific formulation over models based on the Cambridge stress path parameters is that the

stress ratio at failure is independent of the intermediate stress σ_2', hence the model can be applied without modification to different stress paths including triaxial compression and extension. While Eq. (5) is obviously an approximation of true soil response, it provides a simple and cost-effective yield criterion for frictional materials.

The hardening rule can be expressed in differential form using the total derivative:

$$d\gamma^p = \frac{1}{G^{p^*}} d\eta_{mob} = \frac{1}{G^{p^*} p_M'} \left(-\eta_{mob} dp_M' + dq_M \right) \tag{6}$$

where G^{p^*} is a dimensionless plastic shear modulus relating $d\gamma^p$ and $d\eta$. In the realm of the specific model, G^{p^*} is estimated from the empirical relation in Eq. (7):

$$G^{p^*} = k_G^p \left(\frac{p_M'}{p_a}\right)^{np} \left(1 - \frac{\eta_{mob}}{\eta_f/R_f}\right)^2 \tag{7}$$

where k_G^p is a dimensionless plastic shear modulus parameter (equal to G^{p^*} at $p_M' = p_a$ and $\eta_{mob} = 0$), and η_f is the stress ratio at failure. R_f is the failure ratio adjustment for preventing the over-prediction of strength at failure [2,41]. The plastic shear modulus exponent *np* is usually selected in the range 0.4–0.7 [28] The specific value can be determined from the undrained stress path and the quasi steady-state locations with different consolidation stress [42,43].

The flow rule is of the non-associative type and is given by the following simple formula:

$$\frac{d\varepsilon_v^p}{d\gamma^p} = \eta_{cv} - \eta_{mob} \tag{8}$$

where η_{cv} is the stress ratio under constant volume. A graphical illustration of the UBCSAND hardening and flow rules, mathematically expressed by Eqs. (6) and (8) respectively, is provided in Fig. 1.

By combining Eqs. (6) and (8), the plastic strain increment can be expressed as

$$\begin{bmatrix} d\varepsilon_v^p \\ d\gamma^p \end{bmatrix} = \frac{1}{G^{p^*} p_M'} \begin{bmatrix} -\eta_{mob}(\eta_{cv} - \eta_{mob}) & \eta_{cv} - \eta_{mob} \\ -\eta_{mob} & 1 \end{bmatrix} \begin{bmatrix} dp_M' \\ dq_M \end{bmatrix} \tag{9}$$

Adding Eqs. (4b) and (9), the combined elastic and plastic volumetric and shear strain increments are obtained from the equation:

$$\begin{bmatrix} d\varepsilon_v \\ d\gamma \end{bmatrix} = \begin{bmatrix} C_{11} & C_{12} \\ C_{21} & C_{22} \end{bmatrix} \begin{bmatrix} dp_M' \\ dq_M \end{bmatrix} \tag{10}$$

where

$$C_{11} = \frac{1}{K^e} + \frac{-\eta_{mob}(\eta_{cv} - \eta_{mob})}{G^{p^*} p_M'} \tag{11a}$$

$$C_{12} = \frac{-1}{3K^e} + \frac{\eta_{cv} - \eta_{mob}}{G^{p^*} p_M'} \tag{11b}$$

$$C_{21} = \frac{-\eta_{mob}}{G^{p^*} p_M'} \tag{11c}$$

$$C_{22} = \frac{1}{G^e} + \frac{1}{G^{p^*} p_M'} \tag{11d}$$

are the elements of the compliance matrix. Explicit formulae obtained upon substituting Eq. (7) into Eq (11) are provided in Appendix C.

Since parameters ν, *ne* and *np* are often selected empirically [28,31, 37,38,40,42–46], without a rigorous calibration, the above model involves four main dimensionless parameters that need to be calibrated against problem-specific data: k_G^p, k_G^p/k_G^e, η_f/R_f and η_{cv}. Parameter η_{cv} is exclusively related to the plastic volumetric strain increment $d\varepsilon_v^p$ as evident from Eq. (9).

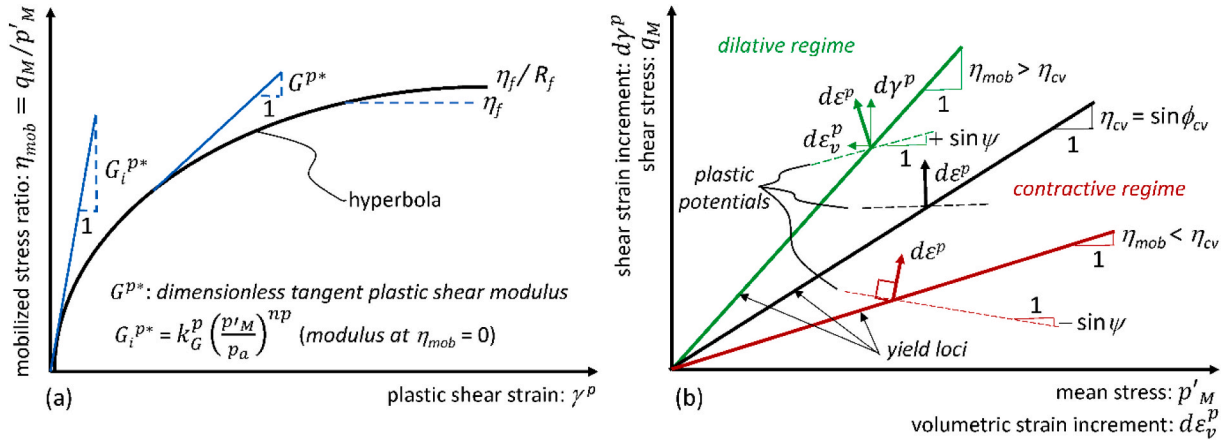The stress increments are obtained from the stiffness formulation in

Fig. 1. (a) Hardening rule; (b) Yield criterion and flow rule for UBCSAND model (*modified after* [27]).

Eq. (12):

$$\begin{bmatrix} dp'_M \\ dq_M \end{bmatrix} = \begin{bmatrix} D_{11} & D_{12} \\ D_{21} & D_{22} \end{bmatrix} \begin{bmatrix} d\varepsilon_v \\ d\gamma \end{bmatrix} \tag{12}$$

where

$$D_{11} = \frac{1}{H}\left[\frac{1}{G^e} + \frac{1}{G^{p*}p'_M}\right] \tag{12a}$$

$$D_{12} = \frac{1}{H}\left[\frac{1}{3K^e} - \frac{(\eta_{cv} - \eta_{mob})}{G^{p*}p'_M}\right] \tag{12b}$$

$$D_{21} = \frac{1}{H}\left[\frac{\eta_{mob}}{G^{p*}p'_M}\right] \tag{12c}$$

$$D_{22} = \frac{1}{H}\left[\frac{1}{K^e} - \frac{\eta_{mob}(\eta_{cv} - \eta_{mob})}{G^{p*}p'_M}\right] \tag{12d}$$

in which

$$H = \frac{1}{G^e K^e} - \frac{\eta_{mob}(\eta_{cv} - \eta_{mob})}{G^e G^{p*}p'_M} + \frac{3 - \eta_{mob}}{3K^e G^{p*}p'_M} \tag{12e}$$

in the above equations D_{11}, D_{12}, D_{21} and D_{22} are the elements of the stiffness matrix **D** (inverse of matrix **C** in Eq. (10)). Explicit formulae obtained by substituting Eqs. (1) and (7) into Eq (12) are provided in Appendix C. For drained triaxial compression $\delta q_M = \delta p'_M$; the overall volumetric strain increment can then be obtained from $d\gamma$ as follows:

$$d\varepsilon_v = \left(\frac{D_{22} - D_{12}}{D_{11} - D_{21}}\right)d\gamma \tag{13}$$

The initial shear modulus (G_o) of isotropically consolidated samples under triaxial drained compression ($dq_M = dp'$) can be obtained from terms C_{21} and C_{22} in Eq. (10) as $G_o = dq_M/d\gamma = 1/(C_{21} + C_{22})$. This yields the following solution

$$G_o = \frac{k_G^e k_G^p}{k_G^p\left(\frac{p'_M}{p_a}\right)^{1-ne} + k_G^e\left(\frac{p'_M}{p_a}\right)^{-np}}p'_M \tag{14}$$

where $p_M' (= p_c')$ is the isotropic confining stress. Evidently, since η_{mob} is assumed equal to 0, there is no purely elastic regime so that elastic and plastic strains coexist even at zero deviatoric stress. Accordingly, a combination of parameters k_G^e and k_G^p control the value of G_o; hence k_G^e and k_G^p cannot be uniquely defined by measuring the mechanical properties of the specimen at small strains. Moreover, this finding may explain the dependence of V_s measured using wave methods to the level of the imposed shear strain (recall that dq and dp_M' are proportional for

all oblique stress paths). This finding is in contrast to the calibration procedure suggested by Beaty [31] in which k_G^e is determined directly from V_s values obtained experimentally at low (non-zero) strains. Further, setting $\eta_{mob} = 0^+$ allows for an elastic region in the limit sense, prohibiting plastic deformations ($k_G^P \to +\infty$). Imposing this condition to Eq. (14) yields the anticipated result $G_o = G^e$ according to Eq. (1).

2.2. Analytical integration

The UBCSAND hardening and flow rule differential in Eqs. (6) and (8) can be integrated analytically for different stress paths. Considering triaxial compression and drained conditions, the mean effective stress can be expressed as $p'_M = p'_c + q_M$, where p'_c is the effective confining pressure at zero deviatoric stress. As the stress ratio η is equal to q_M/p'_M, the mean effective stress and the deviatoric stress at the plane of loading can be expressed as functions of η via the equations:

$$p'_M = \frac{1}{1 - \eta}p'_c \tag{15}$$

$$q_M = \frac{\eta}{1 - \eta}p'_c \tag{16}$$

Combining Eq. (16) with Eqs. (1) and (4b), and after some trivial algebraic manipulations, the elastic shear strain increment can be expressed as

$$d\gamma^e = \frac{dq_M}{G^e} = \frac{1}{k_G^e(1-\eta)^{2-ne}}\left(\frac{p'_c}{p_a}\right)^{1-ne}d\eta \tag{17}$$

Integrating the above equation over η yields the elastic shear strain in closed form

$$\gamma^e = \frac{-1}{k_G^e(1-ne)}\left[1 - \frac{1}{(1-\eta)^{1-ne}}\right]\left(\frac{p'_c}{p_a}\right)^{1-ne} \tag{18}$$

expressed as a function of five dimensionless parameters: k_G^e, η, ν, ne and p'_c/p_a.

In the same vein, using Eq. (15) and Eq. (7), Eq. (6) can be expressed in terms of η to give the plastic shear strain increment

$$d\gamma^p = \frac{1}{k_G^p\left(\frac{p'_c}{p_a}\right)^{np}\left(1 - \frac{\eta}{\eta_f/R_f}\right)^2}(1-\eta)^{np}d\eta \tag{19}$$

The above equation can be integrated analytically for the plastic shear strain

$$\gamma^p = \frac{1}{k_G^p \left(\frac{p_c'}{p_a}\right)^{np} (1-np)} \left[\frac{(1-\eta)^{(1+np)}}{\left(1-\frac{\eta}{\eta_f/R_f}\right)^2} {}_2F_1\left[1,2,2-np,\frac{1-\frac{1}{\eta_f/R_f}}{1-\frac{\eta}{\eta_f/R_f}}\right] \right.$$

$$\left. - {}_2F_1\left[1,2,2-np,1-\frac{1}{\eta_f/R_f}\right] \right] \tag{20}$$

where ${}_2F_1$ is the Gaussian hypergeometric function [47]. The hypergeometric function is a special form of power series in a single independent variable x (last term in brackets ${}_2F_1[a,b,c,x]$, with a known general term, which allows analytical integration and differentiation of the function. Due to the complexity of the series and except for a limited number of special cases, no straightforward conclusions as to the behavior of the function can be gleaned by simple inspection of parameters a, b, c, x without direct numerical evaluation of the series. This can be easily done using standard mathematical software. More information is provided in Appendix D.

The elastic volumetric strain can be obtained in a similar manner as the elastic shear strain, by combining Eqs. (15) and (16) with Eq. (4b) to get

$$d\varepsilon_v^e = \frac{dp_M'}{K^e} - \frac{dq_M}{3K^e} = \frac{2p_c'}{3K^e(1-\eta)^2} d\eta \tag{21}$$

Substituting Eqs. (1) and (2) in the above formula and integrating over η, ε_v^e is obtained as:

$$\varepsilon_v^e = \int_0^\eta \frac{1}{k_G^e (1-\eta)^{2-ne}} \frac{(1-2\nu)}{(1+\nu)} \left(\frac{p_c'}{p_a}\right)^{1-ne} d\eta = \frac{-1}{k_G^e} \frac{1}{(1-ne)} \left[1 - \frac{1}{(1-\eta)^{1-ne}}\right] \frac{(1-2\nu)}{(1+\nu)} \left(\frac{p_c'}{p_a}\right)^{1-ne} \tag{22}$$

which is a function of the same dimensionless parameters as γ^e in Eq. (18).

Finally, the plastic volumetric strain can be derived analytically from the flow rule. Indeed, substituting Eq. (19) in Eq. (8) and integrating over η, one gets

$$\varepsilon_v^p = \int_0^\eta \frac{a(1-\eta)^{np}(\eta_{cv}-\eta)}{k_G^p \left(\frac{p_c'}{p_a}\right)^{np} \left(1-\frac{\eta}{\eta_f/R_f}\right)^2} d\eta \tag{23}$$

where a is a fitting parameter typically taken equal to 1. The solution to the above integral is

$$\varepsilon_v^p = \frac{a \, \eta_f/R_f}{k_G^P \left(\frac{p_c'}{p_a}\right)^{np}} (X_1 - X_2 - X_3) \tag{24}$$

where,

$$X_1 = -\frac{\left(1-\frac{\eta_{cv}}{\eta_f/R_f}\right)}{\left(1-\frac{1}{\eta_f/R_f}\right)} \left\{ 1 - \left[1 + \frac{\left(1-\frac{1}{\eta_f/R_f}\right)}{np\left(1-\frac{\eta_{cv}}{\eta_f/R_f}\right)}\right] {}_2F_1\left[1,1,1-np,1-\frac{1}{\eta_f/R_f}\right] \right\} \tag{25a}$$

$$X_2 = -\frac{\left(\eta_f/R_f\right)^{(1+np)}\left(1-\frac{\eta_{cv}}{\eta_f/R_f}\right)}{(1-np)\left(1-\frac{\eta}{\eta_f/R_f}\right)^{1-np}} {}_2F_1\left[1-np,-np,2-np,\frac{\left(1-\frac{1}{\eta_f/R_f}\right)}{\left(1-\frac{\eta}{\eta_f/R_f}\right)}\right] \tag{25b}$$

$$X_3 = -\frac{\left(\eta_f/R_f\right)^{(1+np)}}{np\left(1-\frac{\eta}{\eta_f/R_f}\right)^{-np}} {}_2F_1\left[-np,-np,1-np,\frac{\left(1-\frac{1}{\eta_f/R_f}\right)}{\left(1-\frac{\eta}{\eta_f/R_f}\right)}\right] \tag{25c}$$

are dimensionless functions. Like in the solution in Eq. (20), no general conclusions can be gleaned as to the behavior of functions X_1, X_2, X_3 without numerical evaluation of the relevant series. A graphical illustration of Eq. (25) is provided in Appendix D.

The above analysis can be readily extended to other stress paths (such as triaxial extension) but this lies beyond the scope of this work.

As a final remark, integrating over η implies a monotonic increase of η from zero (or a finite value). This stress-controlled loading implies no η-softening. To account for such softening (which is a common trait of the response of dense sands under drained loading), modifications in the analysis would be required which lie beyond the scope of this work.

2.3. Parameter selection

As mentioned in Section 2.1, the dimensionless parameters involved in the model are: k_G^p, k_G^e, η_f/R_f, η_{cv}, ν, ne and np. The last three, ν, ne and np, are often selected empirically and for the purposes of these study we have assumed $\nu = 0.2$, $ne = 0.5$, $np = 0.4$ based on the following brief discussion.

The elastic Poisson's ratio ν is typically selected in the range 0 to 0.2 [2,31] based on studies of small strain elastic response of sands [44]. Recent laboratory experiments have confirmed that ν ranges from 0.1 to 0.3 for different granular materials [45,46]. In this light, the value $\nu \approx$ 0.2 seems reasonable.

In the ensuing, np has been taken equal to 0.4 based on the tested materials and stress conditions. This value is in the range of 0.35–0.65 to include quasi-steady state effects [42,43].

2.4. Errors in numerical integration

Apart from allowing a robust calibration of the model, the analytical treatment at hand allows assessing the error encountered in numerical integration procedures.

To evaluate the numerical errors accumulated using incremental Euler-type methods, a standard Taylor expansion can be employed as follows:

$$f(x) = f(\bar{x}) + f'(\bar{x})(x-\bar{x})^1 + \frac{f''(\bar{x})}{2!}(x-\bar{x})^2 + \ldots + \frac{f^{(N-1)}(\bar{x})}{(N-1)!}(x-\bar{x})^{(N-1)} + R_N \tag{26}$$

where x denotes the independent variable, $\bar{x}$ denotes the expansion point and R_N the residual.

Considering up to second derivatives, shear strain can be approximated as

$$\gamma(\eta + d\eta) \approx \gamma(\eta) + \frac{\partial \gamma(\eta)}{\partial \eta} d\eta + \frac{1}{2} \frac{\partial^2 \gamma(\eta)}{\partial \eta^2} d\eta^2 \tag{27}$$

Since Eq. (10) only involves first derivatives, the numerical error is approximately

$$d\gamma_{error} \approx \frac{1}{2}\frac{\partial^2 \gamma(\eta)}{\partial \eta^2}d\eta^2 \tag{28}$$

By establishing the relevant derivatives from Equations (6) and (17), the following formula is obtained:

$$d\gamma_{error} \approx \left[\frac{2-ne}{2}\frac{(1-\eta)^{ne-3}}{k_G^e}\left(\frac{p_c'}{p_a}\right)^{1-ne} + \frac{(1-\eta)^{np}}{2k_G^p\left(\frac{p_c'}{p_a}\right)^{np}}\frac{\frac{2}{\eta_f/R_f}-\frac{np}{1-\eta}\left(1-\frac{\eta}{\eta_f/R_f}\right)}{\left(1-\frac{\eta}{\eta_f/R_f}\right)^3}\right]d\eta^2 \tag{29}$$

The above equation indicates that the prediction error increases both with increasing $d\eta$ and decreasing k_G^e, k_G^p.

The prediction error in assessing ε_v using Eq. (10) can be likewise approximated from Eqs. (22) and (23) as follows:

$$d\varepsilon_{verror} \approx \left\{ \frac{(2-ne)(1-2\nu)}{2(1+\nu)}\frac{(1-\eta)^{ne-3}}{k_G^e}\left(\frac{p_c'}{p_a}\right)^{1-ne} - \frac{a(1-\eta)^{np}\left[\frac{np}{1-\eta}(\eta_{cv}-\eta)+1\right]}{2k_G^p\left(\frac{p_c'}{p_a}\right)^{np}\left(1-\frac{\eta}{\eta_f/R_f}\right)^2} + \frac{a(1-\eta)^{np}\left(\frac{\eta_{cv}-\eta}{\eta_f/R_f}\right)}{k_G^p\left(\frac{p_c'}{p_a}\right)^{np}\left(1-\frac{\eta}{\eta_f/R_f}\right)^3}\right\}d\eta^2 \tag{30}$$

Evidently, the error in ε_v also increases with increasing $d\eta$ and decreasing k_G^e, k_G^p. Fig. 2 shows a comparison of numerical and analytical solutions for (a) q_M vs. γ and (b) ε_v vs. γ, respectively. These results are obtained from Eq. (10) using Euler integration, and Eqs. (18), (20), (22) and (24) for the analytical solution. The figure confirms that the numerical solution deviates from the analytical one as the numerical step in the stress ratio $d\eta$ increases, yet the error is small for $d\eta$ less than 10^{-2} or so.

The errors predicted using the approximate approach summarized in Eqs. (29) and (30), are compared to the errors observed in Fig. 2 by comparing the full numerical solution to the analytical.

Fig. 3(a, c) and (b, d) provides the γ_{error} and ε_{verror}, respectively, against η, for two sets of input parameters. γ_{error} and ε_{verror} cannot be normalized with η_f/R_f, which is also evident from the form of Eqs. (29) and (30). The γ_{error} is positive (Fig. 3a, c), which means that the numerical solution underestimates the analytical one. This is anticipated because the tangent stiffness decreases with η. The ε_{verror} is negative (Fig. 3b, d) showing that the numerical solution overestimates the volumetric strains. This trend is also anticipated by inspecting Eq. (8) in which volumetric strains decrease with η.

The γ_{error} substantially increases when $\eta = 0.5$–0.57 and 0.4–0.5 with $d\eta = 0.01$ and 0.03, respectively (Fig. 3a, c). This observation indicates that the more accurate results are obtained with $d\eta = 0.01$ with higher η.
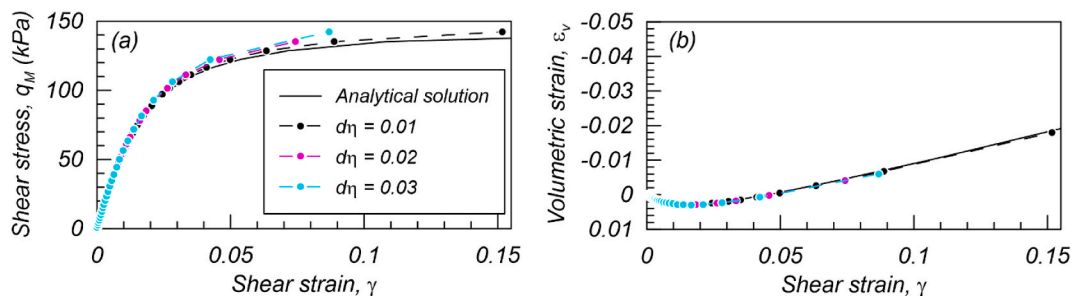
Similar trends are observed in ε_{verror} with η in Fig. 3(b,d). The ε_{verror} substantially increases when $\eta = 0.5$–0.57 and 0.4–0.5 with $d\eta = 0.01$ and 0.03, respectively (Fig. 3a, c). These observations indicate that the selection of $d\eta$ becomes important as η increases.

Fig. 4 illustrates this comparison with the predicted errors plotted versus the observed errors in the x- and y-axes respectively. Model parameters vary as follows: k_G^p from 75 to 300, η_f/R_f from 0.51 to 0.75, and η_{cv} from 0.50 to 0.65. Fig. 4(a) shows that Equation (29) overestimates the observed error when $d\gamma_{error}/d\eta^2$ is smaller than 1. On the other hand, Fig. 4(b) shows that Eq. (30) deviates from the observed error when $|d\varepsilon_{v\text{-}error}|/d\eta^2$ is smaller than 0.1. These observations indicate that higher order approximations via Taylor's expansion are required to assess the numerical error in the integration of the model. Nevertheless, Eqs. (29) and (30) predict reasonably well the numerical errors when the aforementioned dimensionless ratios are greater than 0.1.

Fig. 5(a) and (b) depict the variation of $d\eta$ against η for numerical prediction errors $d\gamma_{error} = 10^{-4}$ and $d\varepsilon_{v\text{-}error} = 10^{-4}$, respectively, calculated using Eqs. (29) and (30). Four k_G^p values were considered: 30, 100, 250, 500, while k_G^p/k_G^e, η_f/R_f and η_{cv} were kept constant at 0.83, 0.75 and 0.55, respectively. The figure shows that $d\eta$ decreases as k_G^p decreases and that the variation differs between the prediction errors for shear and volumetric strain. For example, Fig. 5(a) shows that $d\eta = 0.004$ and 0.018 when $k_G^p = 30$ and 500, respectively, for $\eta = 0.6$. On the other hand, Fig. 5(b) shows that $d\eta = 0.013$ and 0.054 when $k_G^p = 30$ and 500, respectively, for $\eta = 0.6$. The peak value observed around 0.43 corresponds to the point where $f(\eta) = 0$ as $d\varepsilon_{verror} \approx f(\eta)d\eta^2$ is, by definition, greater than zero. Using Eqs. 29 and 30 and Fig. 5, the $d\eta$ value can be selected to limit the numerical error in the integration of UBC-SAND via Eq. (10).

3. Calibration procedures

3.1. Chart solution

A graphical solution is proposed for calibrating k_G^p, k_G^p/k_G^e, η_f/R_f and η_{cv} from isotropic consolidated drained monotonic compression tests. In the calibrations, three parameters are kept constant: $\nu = 0.2$, $ne = 0.5$, and $np = 0.4$. Fig. 6 shows stress-strain (η vs. γ) curves obtained by numerical integration of Eq. (10) for different combinations of k_G^p,

Fig. 2. Comparison between analytical (solid lines) and numerical (dots) solutions for different sizes of the numerical step $d\eta$: (a) q_M vs. γ, (b) ε_v vs. γ; $\eta_f/R_f = 0.747$, $k_G^p/k_G^e = 0.83$, $k_G^p = 250$, $\eta_{cv} = 0.55$, $\nu = 0.2$, $ne = 0.5$, $np = 0.4$, $p_c' = 50$ kPa.
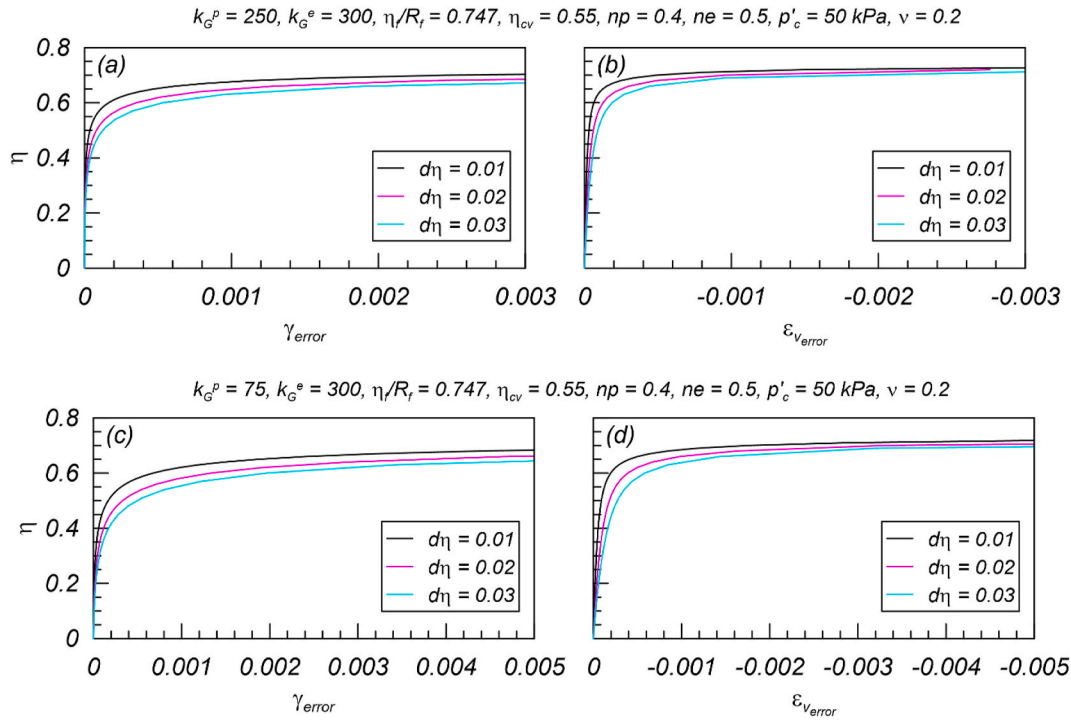
Fig. 3. Numerical errors in shear (a, c) and volumetric (b, d) strains for different sizes of the numerical step $d\eta$ ($k_G^p = 250$ (a, b) and 75 (c, d), $k_G^e = 300$, $\nu = 0.2$, $ne = 0.5$, $np = 0.4$, $p'_c = 50$ kPa, $\eta_{cv} = 0.55$, $\eta_f/R_f = 0.747$).
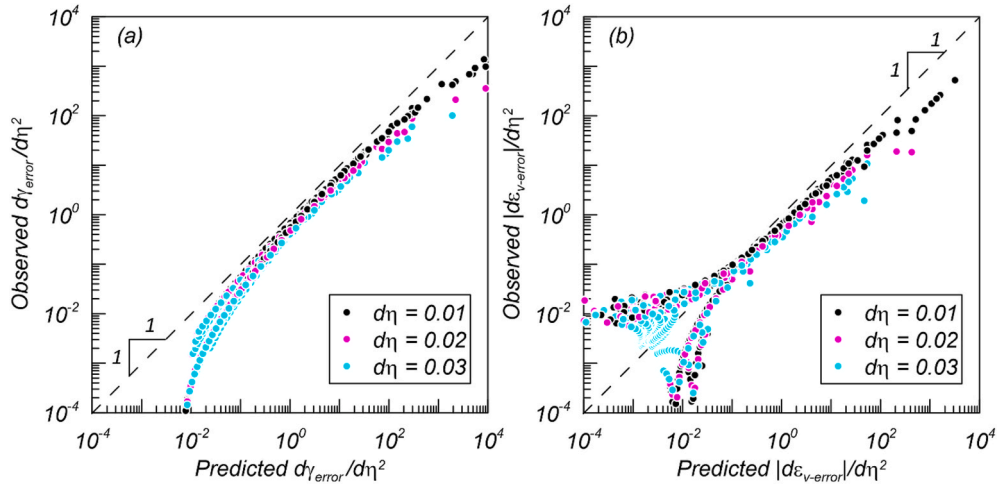

Fig. 4. Prediction errors of the numerical approach (Eq. (10)) against analytical solutions (Eqs. (29 and 30)) for different sizes of the numerical step $d\eta$: (a) $d\gamma_{error}/d\eta^2$, (b) $|d\varepsilon_{v-error}|/d\eta^2$. η_f/R_f, k_G^p/k_G^e and η_{cv} range from 0.51 to 0.75, 0.25 to 1.0, and 0.50 to 0.65, respectively; $\nu = 0.2$, $ne = 0.5$, $np = 0.4$, $p'_c = 50$ kPa and $k_G^e = 300$.

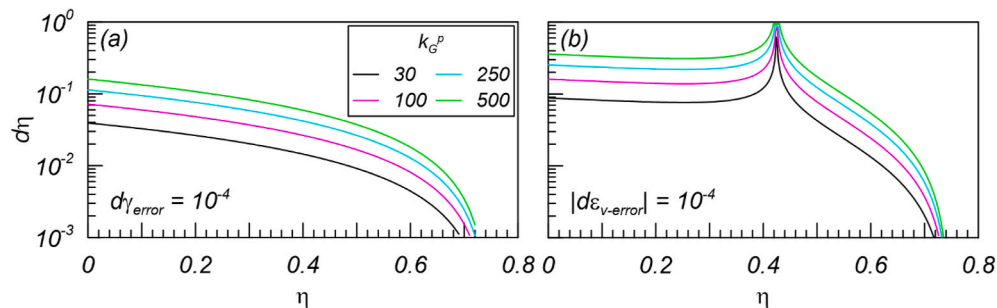**Fig. 5.** Variation in $d\eta$ against η with different k_G^p for numerical prediction errors in strain using second-order Taylor expansion (Eq. (29), (30)): (a) $d\gamma_{error} = 10^{-4}$, (b) $d\varepsilon_{v-error} = 10^{-4}$. $\eta_f/R_f = 0.747$, $k_G^p/k_G^e = 0.83$, $\eta_{cv} = 0.55$, $\nu = 0.2$, $ne = 0.5$, $np = 0.4$, $p'_c = 50$ kPa.

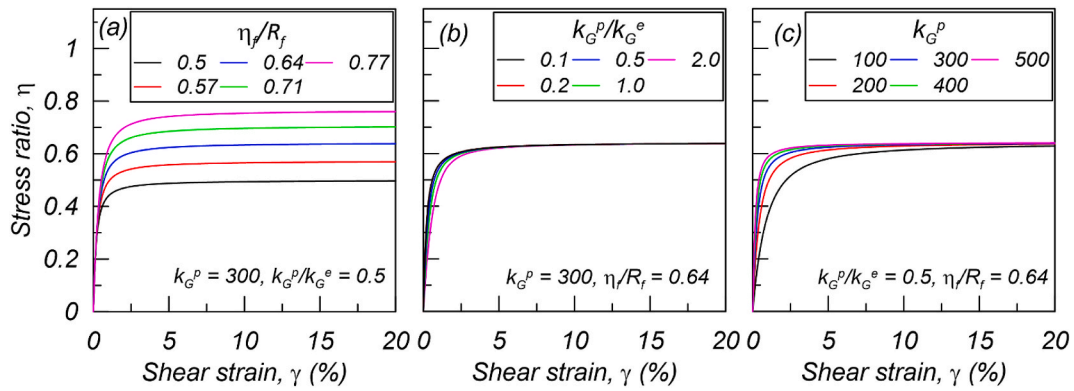**Fig. 6.** Variations of stress-strain curves for drained compression for (a) η_f/R_f, (b) k_G^p/k_G^e, and (c) k_G^p; In all simulations $p'_c = 100$ kPa.
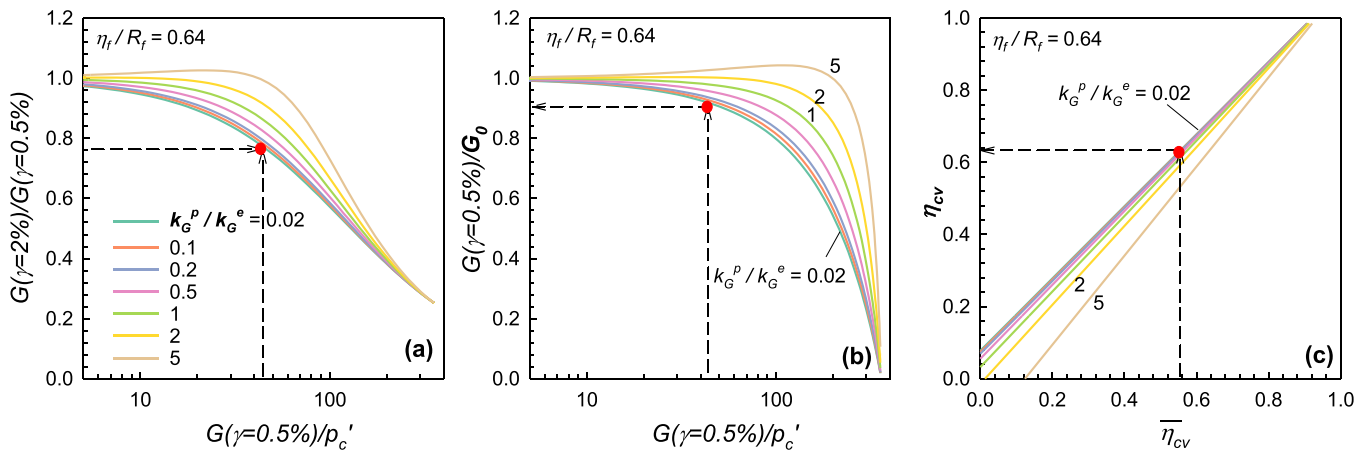

Fig. 7. (a) Estimation of k_G^p/k_G^e from variations in normalized secant modulus; (b) Estimation of G_o; (c) Estimation of η_{cv}. In all simulations $p'_c = 100$ kPa.

k_G^p/k_G^e, and η_f/R_f values. The failure strength is controlled by η_f/R_f, while k_G^p and k_G^p/k_G^e control the shape of the curves and do not significantly affect η_f/R_f. Accordingly, one only needs to determine η_f/R_f from the experimental results in order to properly calibrate the other model parameters using the chart solution.

An example of the proposed chart solution is illustrated in Fig. 7. Fig. 7(a) shows the variation in secant shear modulus (G) at $\gamma = 0.5\%$ and 2% for different k_G^p/k_G^e values, $p'_c = 100$ kPa, and $\eta_f/R_f = 0.64$. Fig. 7 (b) shows the variation of $G(\gamma = 0.5\%)/G_o$ for different values of k_G^p/k_G^e. Both Fig. 5 (a) and (b) were created numerically from Eq. (10).

The ratio k_G^p/k_G^e can be uniquely determined if G is available (i.e.

Table 1
Step-by-step UBCSAND calibration methodology using the proposed chart solution.

Steps	
1	Select values for ν, ne, np
2	Determine η_f/R_f from laboratory test results
3	In Appendix B choose the chart solution corresponding to the determined η_f/R_f
4	Determine $G(\gamma = 0.5\%)$, $G(\gamma = 2\%)$ from laboratory test results. Determine k_G^p/k_G^e from Figures (a)[a] in Appendix B.
5	For the determined k_G^p/k_G^e and known $G(\gamma = 0.5\%)$ determine G_o from Figures (b)[a] in Appendix B.
6	From Eq. (31) and using the values of k_G^p/k_G^e and G_o (from steps 4 & 5) calculate k_G^p
7	Calculate $\overline{\eta}_{cv}$ from Eq. (32) and from Figures (c) in Appendix B determine η_{cv}

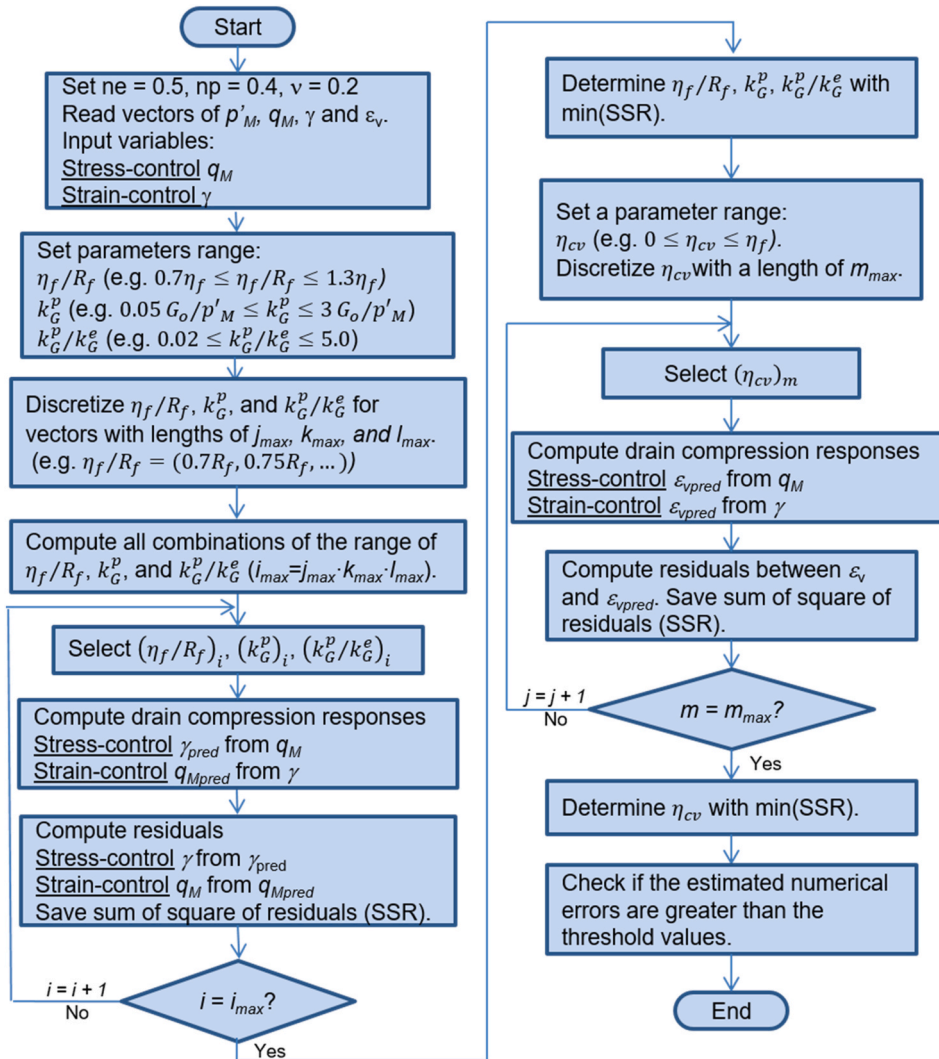[a] Figures (a) and (b) in Appendix B were numerically created from Eq. (10).

from experimental data) at $\gamma = 0.5\%$ and 2% from Figure 7(a). This indicates that G at different strains can be normalized with k_G^p/k_G^e for a range of k_G^p values, which is anticipated in light of Eqs (10), (11), (18) and (20). The G_o value can then be readily determined from Fig. 7(b) and the known value of G at $\gamma = 0.5\%$. Once k_G^p/k_G^e and G_o are determined the parameter k_G^p can be obtained from Eqs. (14) and (15) for $\eta = 0$, which is re-arranged here as follows

$$k_G^p = \frac{G_o}{p'_c}\left[\frac{k_G^p}{k_G^e}\left(\frac{p'_c}{p_a}\right)^{1-ne} + \left(\frac{p'_c}{p_a}\right)^{-np}\right] \tag{31}$$

Fig. 7(c) shows the variation in η_{cv} with the estimated approximate value $\overline{\eta}_{cv}$ for different k_G^p/k_G^e ratios. $\overline{\eta}_{cv}$ is an approximate index obtained from the stress-strain curves using Eq. (8) as follows:

$$\overline{\eta}_{cv} = \frac{\varepsilon_v(\eta = 0.95\eta_f/R_f) - \varepsilon_v(\eta = 0.55\eta_f/R_f)}{\gamma(\eta = 0.95\eta_f/R_f) - \gamma(\eta = 0.55\eta_f/R_f)} + 0.75\eta_f/R_f \tag{32}$$

As the influence of k_G^p on $\overline{\eta}_{cv}$ is minor, Fig. 7(c) properly represents the normalized response. The figure shows that the relation between $\overline{\eta}_{cv}$ and η_{cv} varies slightly with k_G^p/k_G^e. Evidently, η_{cv} decreases for a given $\overline{\eta}_{cv}$ as k_G^p/k_G^e increases, because elastic strains become larger relative to plastic. Since k_G^p/k_G^e is available from the $\eta - \gamma$ relationship in Fig. 7(a), η_{cv} can be readily obtained from Fig. 7(a) and Eq. (32). A step – by – step methodology for the proposed chart solution is provided in Table 1.

Additional charts are provided in Appendix B for different values of η_f/R_f, p'_c, k_G^p/k_G^e, and η_{cv}. Using these charts, the parameters η_f/R_f, k_G^p, k_G^p/k_G^e, and η_{cv} can be determined for a wide range of isotropically

Fig. 8. Flowchart of proposed calibration algorithm of parameters η_f/R_f, k_G^p/k_G^e, k_G^p, η_{cv}.

consolidated drained compression tests.

3.2. Numerical calibration

The prediction errors discussed in the numerical integration section can be minimized and the robustness of the numerical calibration can be improved. Fig. 8 presents a flowchart of the proposed procedure. For stress-controlled tests, the input variables are the vectors of q_M values obtained from experimental results. For strain-controlled tests, the input variables are the vectors of γ values. The experimental data need to have small sampling steps to produce stress increments $d\eta$ smaller than the minimum value established by Eqs. (28) and (29).

Initially, the soil response is numerically predicted by Eqs (10) and (12). The parameters k_G^p, k_G^p/k_G^e, η_f/R_f and η_{cv} are then re-determined by minimizing the prediction errors. A check is included at the end, that the expected errors are smaller than a predetermined threshold value. In this procedure the selection of η_{cv} is independent of the selection of η_f, because η_{cv} is uniquely determined from the η_f/R_f ratio. This framework is different from the calibration procedure suggested by Beaty [31] which focuses on cyclic rather than monotonic behavior.
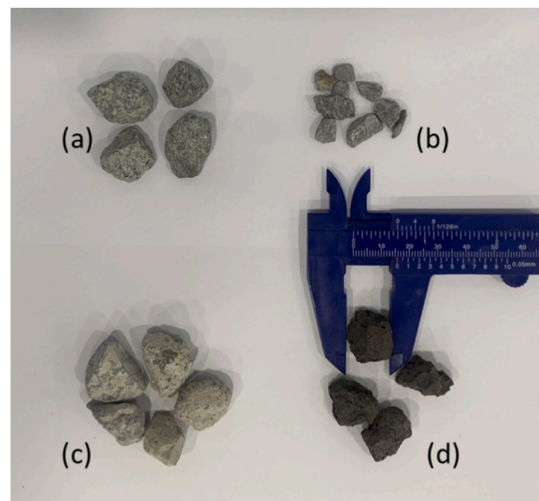

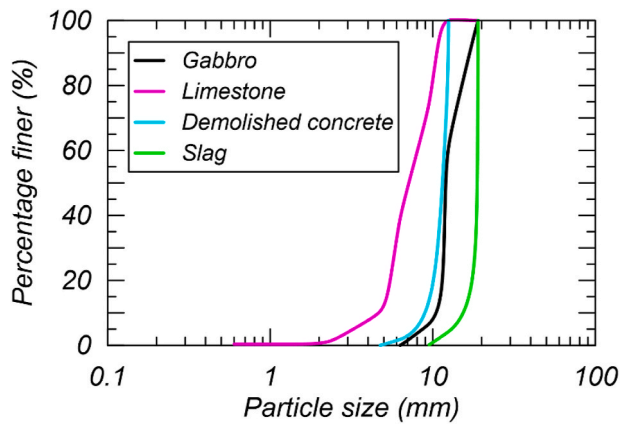**Fig. 9.** Photographs of tested materials (a) gabbro, (b) limestone, (c) demolished concrete, (d) slag.

Fig. 10. Grain size distribution curves of tested materials.

Table 2
Summary of tested materials.

Material	D_{10} (mm)	C_u	Particle shape	Mineralogy
Gabbro	9.7	1.3	Sub-rounded	Coarse-grained silicate
Limestone	4.6	1.7	Angular	Calcium carbonate
Demolished concrete	6.7	1.4	Sub-rounded	Calcium carbonate, silicate aggregate
EAF Slag	12.8	1.3	Sub-angular	Calcium and iron oxide

4. Application to drained monotonic & cyclic tests

4.1. Test materials

The experiments carried out in the Geotechnical Materials Lab at Khalifa University involved four different types of aggregates: (a) gabbro; (b) limestone; (c) demolished concrete; and (d) electric arc furnace (EAF) slag. Gabbro is a coarse grain igneous rock that is rich in iron, magnesium and calcium, and is extracted at the border between UAE and Oman. It is a strong material which is suitable for construction. Limestone is a sedimentary rock made of calcium carbonate, and is available throughout the UAE. It is weaker than gabbro, but also suitable for construction and provides excellent drainage when used as ballast. Demolished concrete is a recycled material - a mixture of cement and aggregates. The cement is weak and crushable. More than 29 million tons of cement are produced annually in the UAE [48]. Slag is a by-product of smelting generated as industrial waste during steel-making process. Slag is stronger and more resilient than the other three materials. More than 800,000 tons of slag are annually produced in the UAE [49].

Fig. 9 shows photographs of the particles of the tested aggregates. Gabbro and demolished concrete particles are rounded, whereas limestone and slag have sharp angular shapes. Fig. 10 and Table 2 present grain-size distribution curves and their characteristics. The angularity of the particles was determined based on sphericity-roundness comparison chart [50]. All materials show uniform gradations. The effective grain size (D_{10}) ranges from 4.6 to 12.8 mm, whereas the coefficient of uniformity (C_u) ranges from 1.3 to 1.7. Such uniform gradations are suitable for construction materials as the exhibit dilatant behavior under both static and cyclic loads [51].

4.2. Test procedure

Triaxial tests were conducted using a GCTS Testing System device (Model No.: SSC-2K-0000). The specimen diameter was 70 mm that is more than 5 times larger than the maximum particle size. Although the particle diameter is large compared to the size of the specimen this is not unusual when gravelly aggregates are tested where d/D varies from 1/4 to 1/5.7 [52]. The specimen height was 150 mm and was built under 20 kPa vacuum, enclosed in a rubber membrane with 0.6 mm thickness. All samples were prepared with the void ratio ranging from 0.5 to 0.8, and were saturated under back pressure with a B-value greater than 0.95. The membrane penetration correction was conducted assuming isotropic behavior during the consolidation stage [53]. The tests were conducted in three stages:

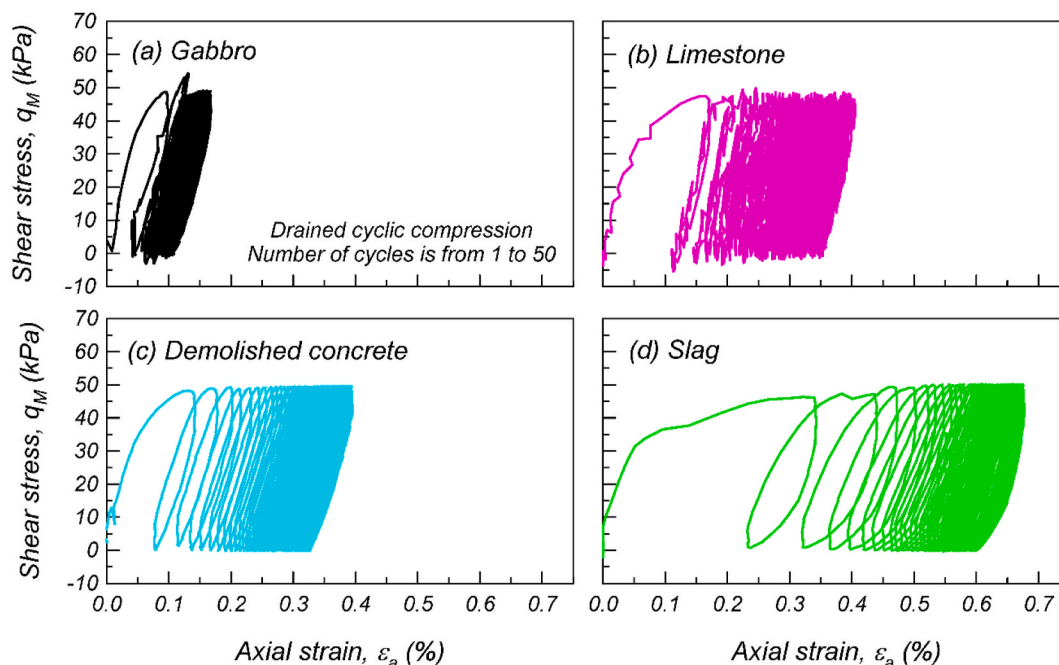Stage 1) Isotropic consolidation under confining stress $\sigma'_c = 50$ kPa.

Fig. 11. Drained cyclic compression test results: (a) Gabbro, (b) Limestone, (c) Demolished concrete, (d) Slag. In all tests $\sigma'_c = 50$ kPa, $q_M = 50$ kPa.
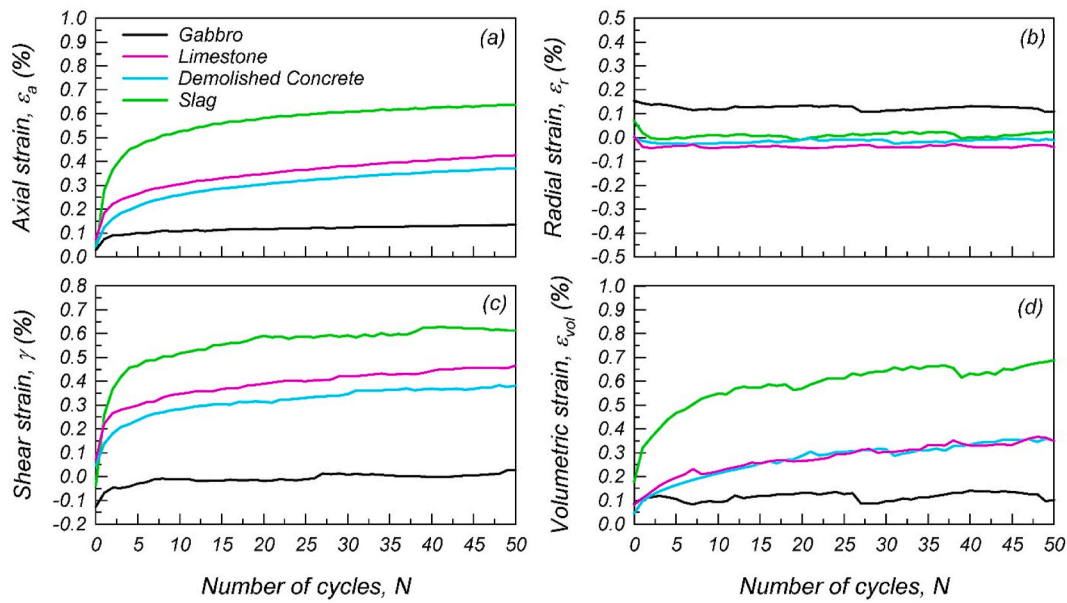
Fig. 12. Cyclic drained compression test results for different materials: (a) ε_a vs. N, (b) ε_r vs. N (d) γ vs. N. In all tests $\sigma'_c = 50$ kPa, $q_M = 50$ kPa.
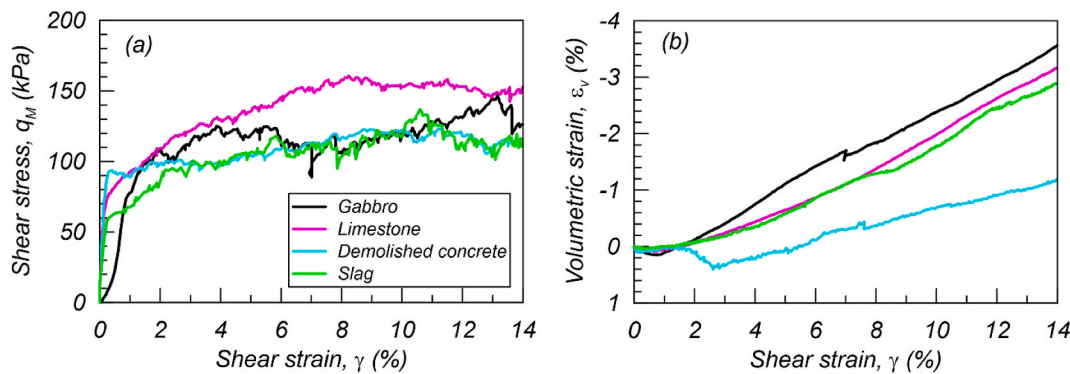
Fig. 13. Monotonic drained compression test results for different materials (a) q_M vs. γ (b) ε_v vs. γ.

Table 3

Calibrated UBCSAND parameters against drained monotonic triaxial compression data for four different ballast aggregates using the three methods described in this paper ($\sigma'_c = 50$ kPa).

Material	Method	k_G^p	k_G^p/k_G^e	η_f/R_f	η_{cv}
Gabbro	Analytical	500	2.00	0.75	0.42
	Chart	234	2.00	0.73	0.36
	Numerical	620	2.77	0.74	0.41
Limestone	Analytical	400	0.10	0.77	0.50
	Chart	720	0.02	0.77	0.53
	Numerical	410	0.10	0.77	0.50
Demolished concrete	Analytical	1000	0.10	0.70	0.60
	Chart	1640	0.02	0.71	0.55
	Numerical	980	0.05	0.68	0.59
EAF Slag	Analytical	300	0.50	0.68	0.42
	Chart	700	0.02	0.68	0.53
	Numerical	320	0.05	0.68	0.44

ne, np, and ν values are fixed at 0.5, 0.4, and 0.2, respectively.

Stage 2) Drained cyclic loading with $q_M = 50$ kPa with a loading frequency of 1 Hz. The applied number of cycles (N) varied from 50 to 200.

Stage 3) Triaxial compression under drained conditions.

The specimen diameter and height were updated for each stage.

4.3. Experimental drained cyclic and monotonic compression measurements

Fig. 11 shows the cyclic loading responses between q_M and axial strain (ε_a) for each material from 1 to 50 cycles. The gabbro testing displayed stiff behavior, whereas slag demonstrated ratcheting. The residual ε_a and volumetric strain (ε_v) against N, is presented in Fig. 12(a) and (b) ε_a and ε_v gradually increase with N, where the slag and the gabbro show the largest and smallest strains, respectively. Limestone and demolished concrete exhibit an intermediate behavior. The accumulation of ε_a and ε_v is similar indicating that the radial strain is limited during cyclic compression. This observation is consistent with previous studies [54], where the radial strain was limited when the amplitude of cyclic load is less than 70% of the static peak strength. In fact, the amplitude of cyclic q_M (Fig. 11) applied in this study was approximately 40% of the static peak strength (Fig. 13). Fig. 13(a) shows a drained monotonic compression response in terms of deviatoric shear stress q_M versus shear strain γ. Limestone exhibits the highest strength (~160 kPa), whereas the other three materials have similar strengths in the range 120–150 kPa. Fig. 13(b) plots ε_v versus γ. The largest and smallest dilatancies were observed in gabbro and demolished concrete, respectively.
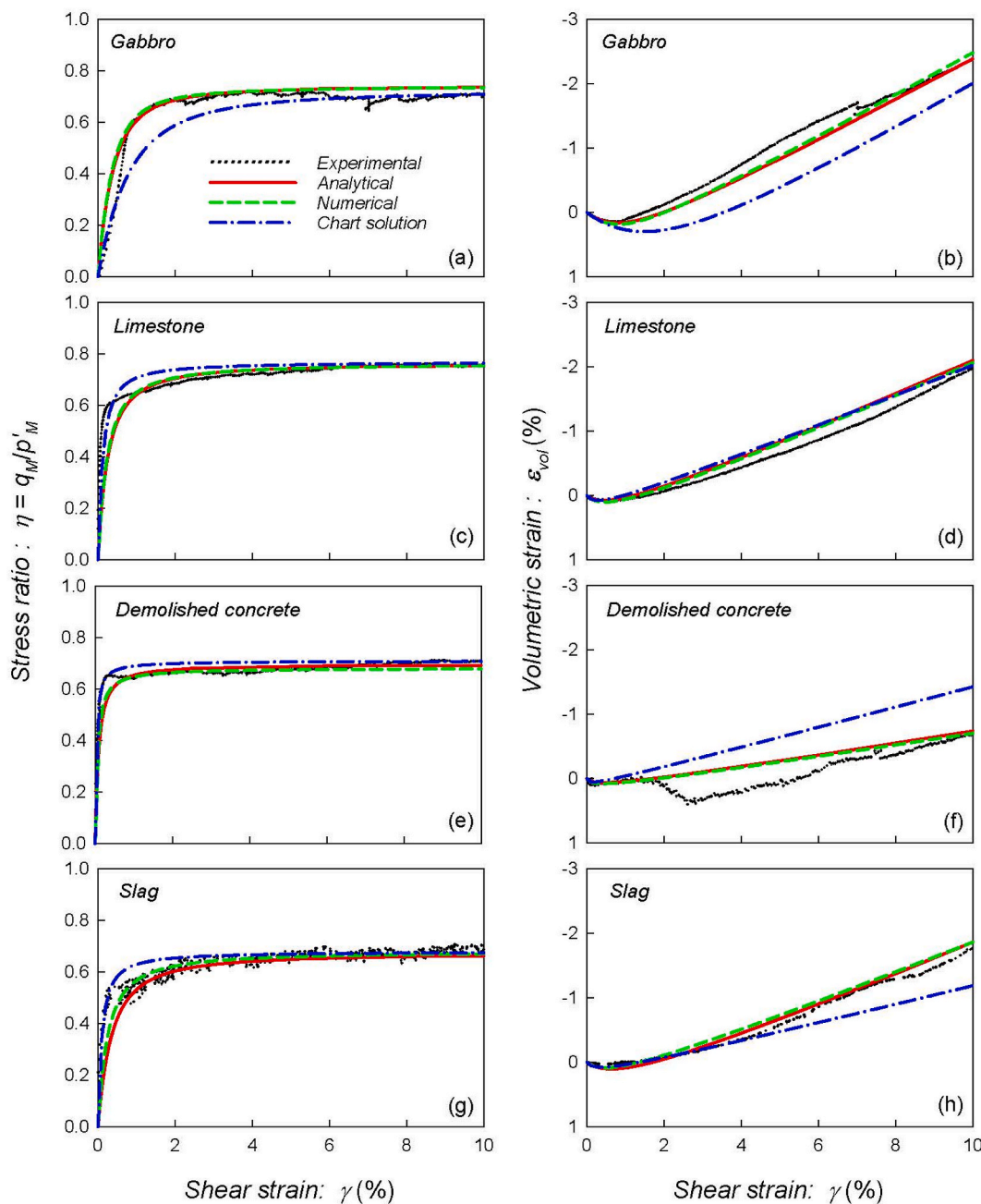
Fig. 14. Calibrated monotonic drained compression tests for four different aggregate materials using the analytical, numerical and chart solutions. The UBCSAND parameters for each case are provided in Table 3. (a) η vs. γ, (b) ε_v vs. γ for gabbro, (c) η vs. γ, (d) ε_v vs. γ for limestone, (e) η vs. γ, (f) ε_v vs. γ for demolished concrete, (g) η vs. γ, (h) ε_v vs. γ for slag.

4.4. Calibration of UBCSAND model to the experimental data

UBCSAND models were calibrated both numerically and analytically using the aforementioned experimental data from drained monotonic compression tests. The numerical procedure for strain-controlled conditions follows Fig. 8. Table 3 provides UBCSAND parameters estimated by employing the three different calibration approaches presented in this study: analytical, chart based, numerical. Fig. 14(a)-(h) presents the calibrated responses of η vs. γ and ε_v vs. γ computed following these approaches. It is demonstrated that the main aspects of the drained monotonic compression response are reproduced adequately by all three methods relative to the experimental data in Fig. 13. The analytical and numerical solutions work best for strains above 1% while the chart solution works best for strains less than 1%.

Fig. 15 shows the example responses of UBCSAND for drained cyclic compression tests of gabbro and slag, using the parameters of numerical calibration in Table 3. The slag simulation exhibits the largest residual ε_a compared to gabbro, which is consistent with the experimental observations in Fig. 11. However, the rate of strain accumulation is constant for UBCSAND, which is different from the experimental findings. Fig. 16 shows the residual values of ε_a and ε_v for drained cyclic compression computed with UBCSAND using the parameters in Table 3. Comparing the results from Figs. 12 and 16, it is fair to mention that the model parameters should be different for cyclic versus monotonic loading, which complicates its application for combinations of static and dynamic loads (a common case in earthquake engineering).

Moreover, the rate of increase of volumetric and shear strains with number of cycles is linear, hence cannot realistically reproduce results
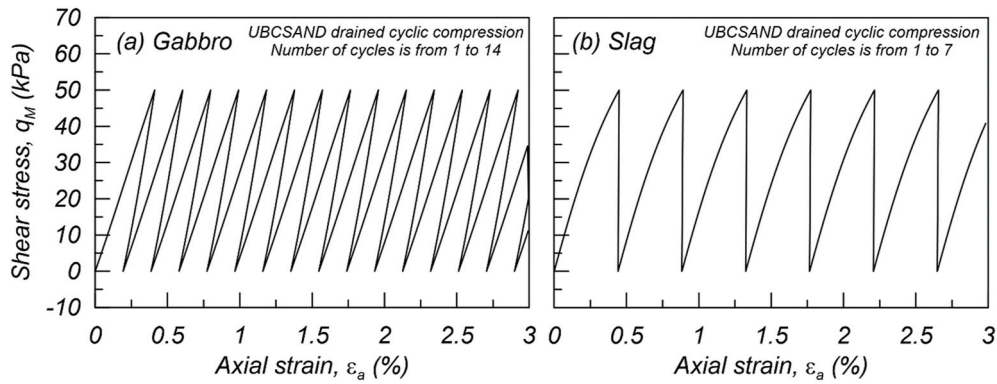
Fig. 15. Example of q_M vs. ε_a cyclic drained response predicted using UBCSAND model based on the calibrated parameters in Table 3: (a) gabbro, (b) slag.
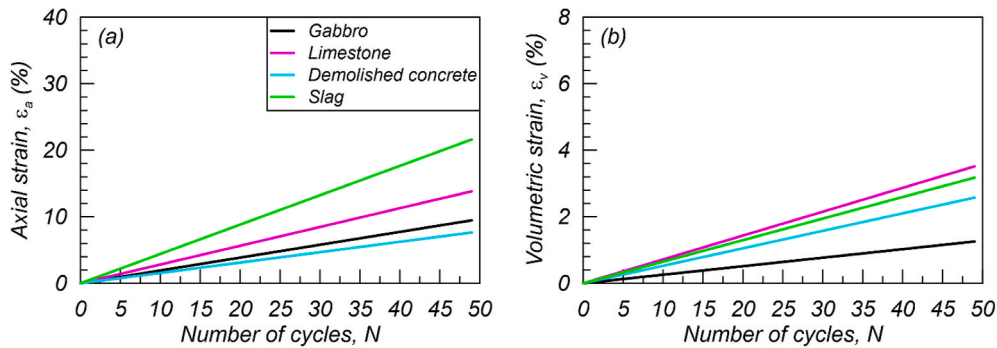

Fig. 16. Examples of residual axial and volumetric strains predicted using UBCSAND for drained cyclic compression response using the calibrated parameters in Table 3: (a) ε_a vs. N; (b) ε_v vs. N ($\sigma'_c = 50$ kPa, $q_M = 50$ kPa).
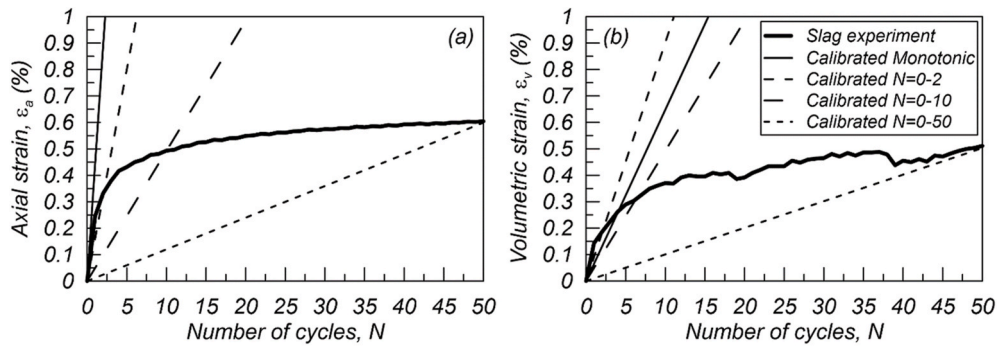

Fig. 17. Comparison of residual strains of slag between experimental and UBCSAND models calibrated based on different loading conditions: (a) N vs. ε_a, (b) N vs. ε_v; $\sigma'_c = 50$ kPa, $q_M = 50$ kPa.

for excess pore pressures under undrained loading. This is evident in Fig. 17 where different calibrations are needed for different number of cycles. These observations are important when trying to apply the specific model to dynamic problems – notably for soil liquefaction analysis.

The UBCSAND model was calibrated against drained cyclic compression tests for different number of loading cycles. Table 4 shows the calibrated parameters for N from 0 to 2, 0 to 10, and 0 to 50 cycles for different materials, respectively. The calibration procedure follows Fig. 8 for stress-controlled conditions. The parameters k_G^p/k_G^e and η_f/R_f are fixed from Table 3 for drained monotonic conditions. The k_G^p/k_G^e

ratio was fixed because the calibrated value was very large (i.e. small k_G^e) due to the plastic deformations developing during successive unloading cycles. η_f/R_f was fixed because it does not provide a reliable value due to the low amplitude of cyclic loads to determine the failure parameters. Table 4 shows that the k_G^p parameter increases as the number of cycles increases. η_{cv} similarly increases as the number of cycles increases when the material exhibits contractive behavior.

Fig. 17 shows the residual strains ε_a and ε_v for slag under drained cyclic tests compared with the calibrated UBCSAND for different loading conditions. The results suggest that the UBCSAND model can be

Table 4
Numerically calibrated UBCSAND parameters against drained cyclic compression tests ($\sigma'_c = 50$ kPa, $q_M = 100$ kPa).

Material	# of cycles N	k_G^p	k_G^p/k_G^e	η_f/R_f	η_{cv}
Gabbro	0–2	5400	2.77	0.74	0.61
	0–10	18,500	2.77	0.74	0.32
	0–50	69,600	2.77	0.74	0.36
Limestone	0–2	1500	0.10	0.77	0.54
	0–10	4800	0.10	0.77	0.74
	0–50	15,900	0.10	0.77	0.86
Demolished concrete	0–2	2900	0.05	0.68	1.00
	0–10	7700	0.05	0.68	1.00
	0–50	25,300	0.05	0.68	0.99
EAF Slag	0–2	760	0.05	0.68	0.50
	0–10	2800	0.05	0.68	0.71
	0–50	11,900	0.05	0.68	0.83

ne, *np*, and *v* values are fixed at 0.5, 0.4, and 0.2, respectively. k_G^p/k_G^e and η_f/R_f values are fixed based on the monotonic compression tests.

reasonably fitted by adjusting the calibration range. The figure also shows that the calibrated parameters against drained monotonic compression tests only predict the cyclic compression responses well when *N* is not larger than 1–4 cycles. Evidently, there is no single set of parameters which can reproduce well both monotonic and cyclic drained conditions.

5. Conclusions

The popular UBCSAND constitutive model was reviewed and integrated analytically for monotonic and cyclic drained triaxial compression. A novel closed form solution for the elastic and plastic shear and volumetric strains was developed. Three new methodologies for calibrating the model parameters to experimental data were proposed: (1) a graphical "chart" solution; (2) a numerical approach based on minimization of residuals; and (3) a trial-and-error approach based on the analytical solution. It has been demonstrated that:

(1) The analytical solution in Eqs. (18), (20), (22), (24) and (25) provides an excellent tool, free of numerical errors, for calibrating the UBCSAND parameters against laboratory data.
(2) The proposed methodology in the flowchart of Fig. 8, efficiently minimizes the errors in the numerical calibration and can be applied for both monotonic and cyclic tests. For good performance it was shown that the experimental data need to have small sampling steps, on the order of 10^{-2} or less in η.
(3) The "chart" solution allows for the graphical determination of the UBCSAND parameters from drained monotonic compression data. For given v, *ne* and *np* values the dimensionless parameters that need to be calibrated are four: k_G^p, k_G^p/k_G^e, η_f/R_f and η_{cv}. η_f/R_f and k_G^p/k_G^e can be uniquely determined from the failure strengths

and the secant modulus. A simple approach to estimate k_G^p and η_{cv} was also proposed.
(4) Results from the numerical calibration against both monotonic and cyclic test data show that the parameters of UBCSAND are different between monotonic and cyclic drained compression conditions. The calibrated parameters against monotonic tests only predict the cyclic compression responses well when *N* is less than 1–4 cycles. Therefore, UBCSAND models should be calibrated against the target loading conditions and number of cycles.

It is fair to mention that the model parameters should be different for cyclic versus monotonic loading, which makes its application for combinations of static and dynamic loads (a most common case in earthquake engineering) difficult. Further, the rate of increase of volumetric and shear strains with number of cycles is always linear, hence cannot realistically reproduce results for excess pore pressures under undrained loading. These observations are important when trying to apply the specific model to dynamic problems – notably in soil liquefaction analysis.

Author statement

All authors have seen and approved the final version of the herein submitted manuscript. The article is the authors' original work, hasn't received prior publication and isn't under consideration for publication elsewhere.

Declaration of competing interest

The authors declare that they have no known competing financial interests or personal relationships that could have appeared to influence the work reported in this paper.

Data availability

Data will be made available on request.

Acknowledgements

APPENDIX A. List of main symbols

Latin symbols	
F	Yield surface
G	Shear modulus
G^e	Elastic shear modulus
G^{p*}	Dimensionless plastic shear modulus
G_o	Initial (maximum) shear modulus
K^e	Elastic bulk modulus
k_G^e	Dimensionless elastic shear modulus parameter
k_G^p	Dimensionless plastic shear modulus parameter
ne	Elastic shear modulus exponent
np	Plastic shear modulus exponent
p'	Cambridge mean effective stress
p_a	Atmospheric pressure
p'_c	Isotropic confining stress
p'_M	MIT mean effective stress in the plane of loading
q	Cambridge deviatoric stress $(\sigma_a - \sigma_r)$
q_M	MIT deviatoric stress in the plane of loading
R_f	Failure ratio
V_s	Shear wave velocity
Greek symbols	
γ	Engineering shear strain
γ^e	Elastic shear strain
γ^p	Plastic shear strain
$d\gamma$	Shear strain increment
$d\gamma_{error}$	Numerical error in shear strain prediction
ε_v	Volumetric strain
ε_v^e	Elastic volumetric strain
ε_v^p	Plastic volumetric strain
$d\varepsilon_v$	Volumetric strain increment
$d\varepsilon_{v_{error}}$	Numerical error in ε_v prediction
η	Stress ratio (q_M/p'_M)
η_{cv}	Stress ratio under constant volume
$\overline{\eta}_{cv}$	Estimated η_{cv} (approximate value)
η_f	Stress ratio at failure
η_{mob}	Mobilized stress ratio
$d\eta$	Stress ratio increment
ν	Poisson's ratio
ξ	Damping ratio
σ'_1	Major effective principal stress
σ'_3	Minor effective principal stress

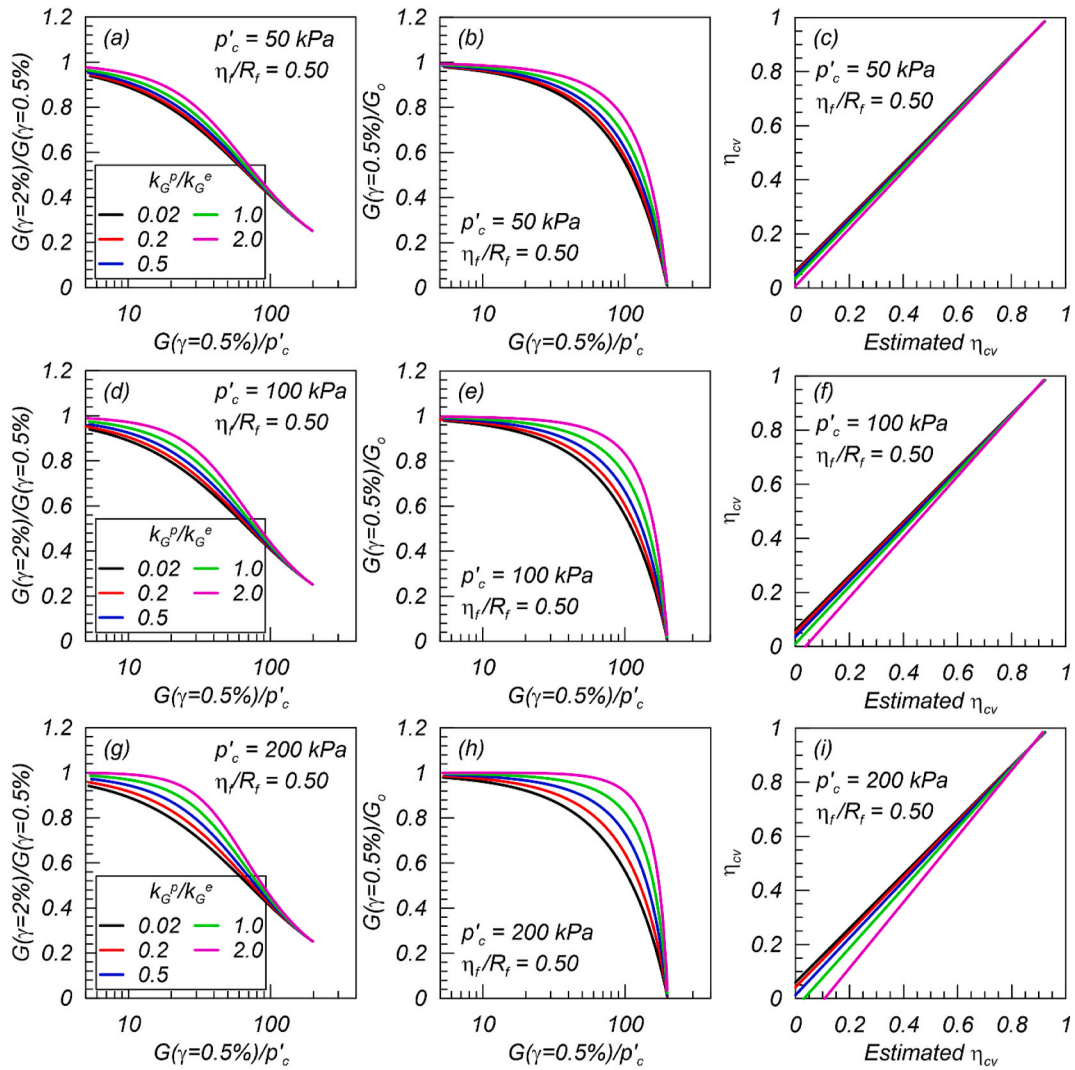## APPENDIX B. "Chart"-based calibration – Additional Figures

Fig. B1. Variations in normalized secant modulus and η_{cv} for different values of k_G^p/k_G^e. ($\eta_f/R_f = 0.50$).
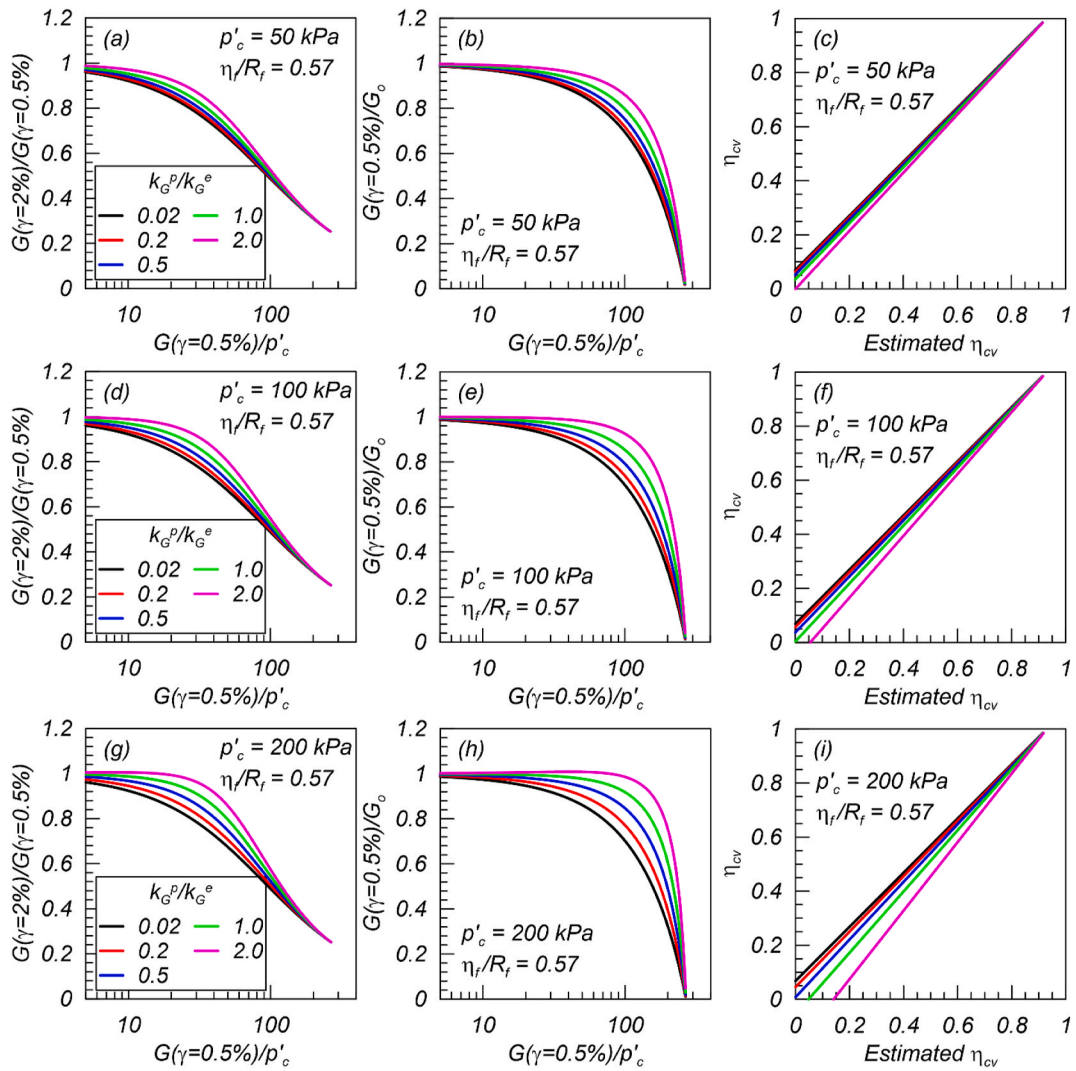
Fig. B2. Variations in normalized secant modulus and η_{cv} for different values of k_G^p/k_G^e. ($\eta_f/R_f = 0.57$).
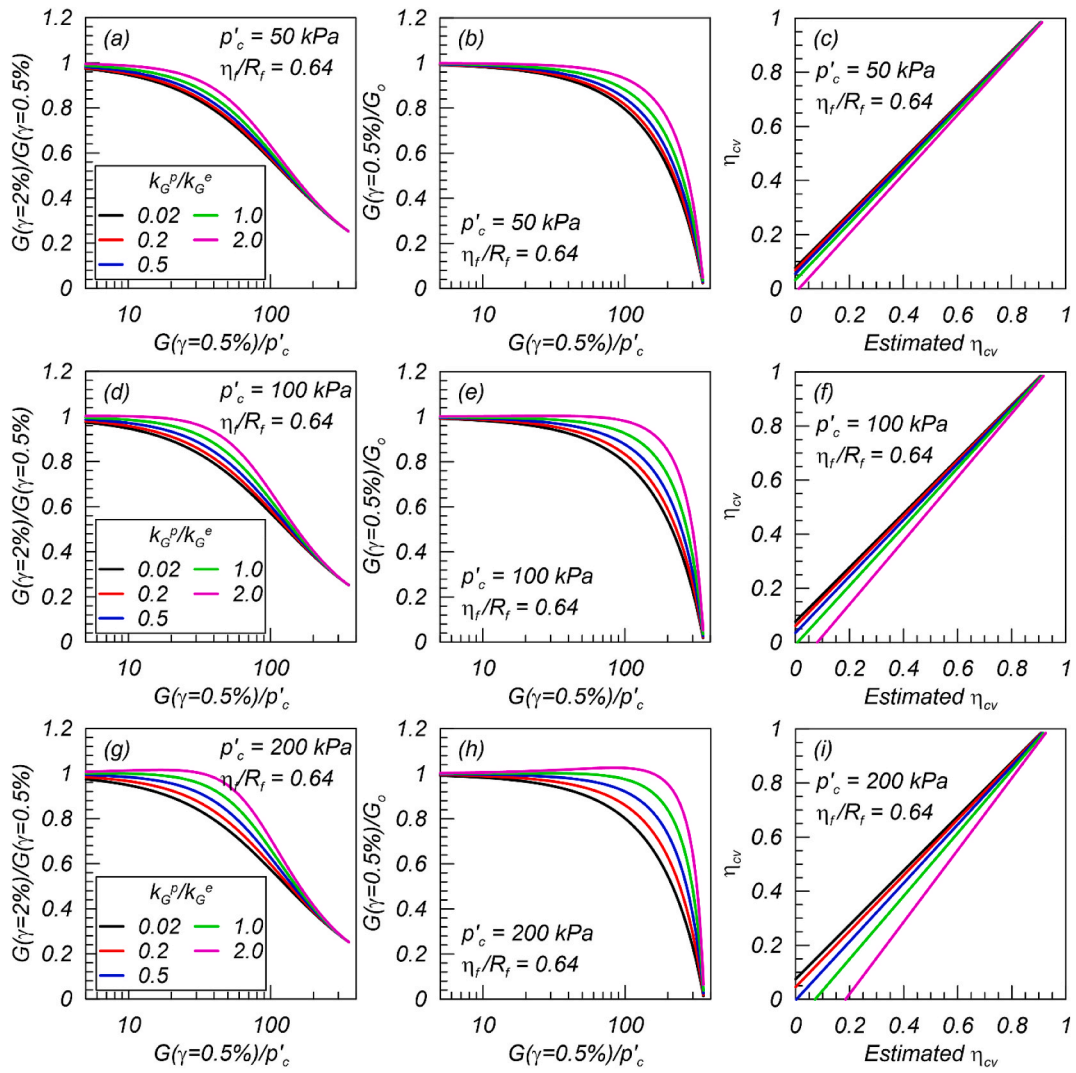
Fig. B3. Variations in normalized secant modulus and η_{cv} for different values of k_G^p/k_G^e. ($\eta_f/R_f = 0.64$).
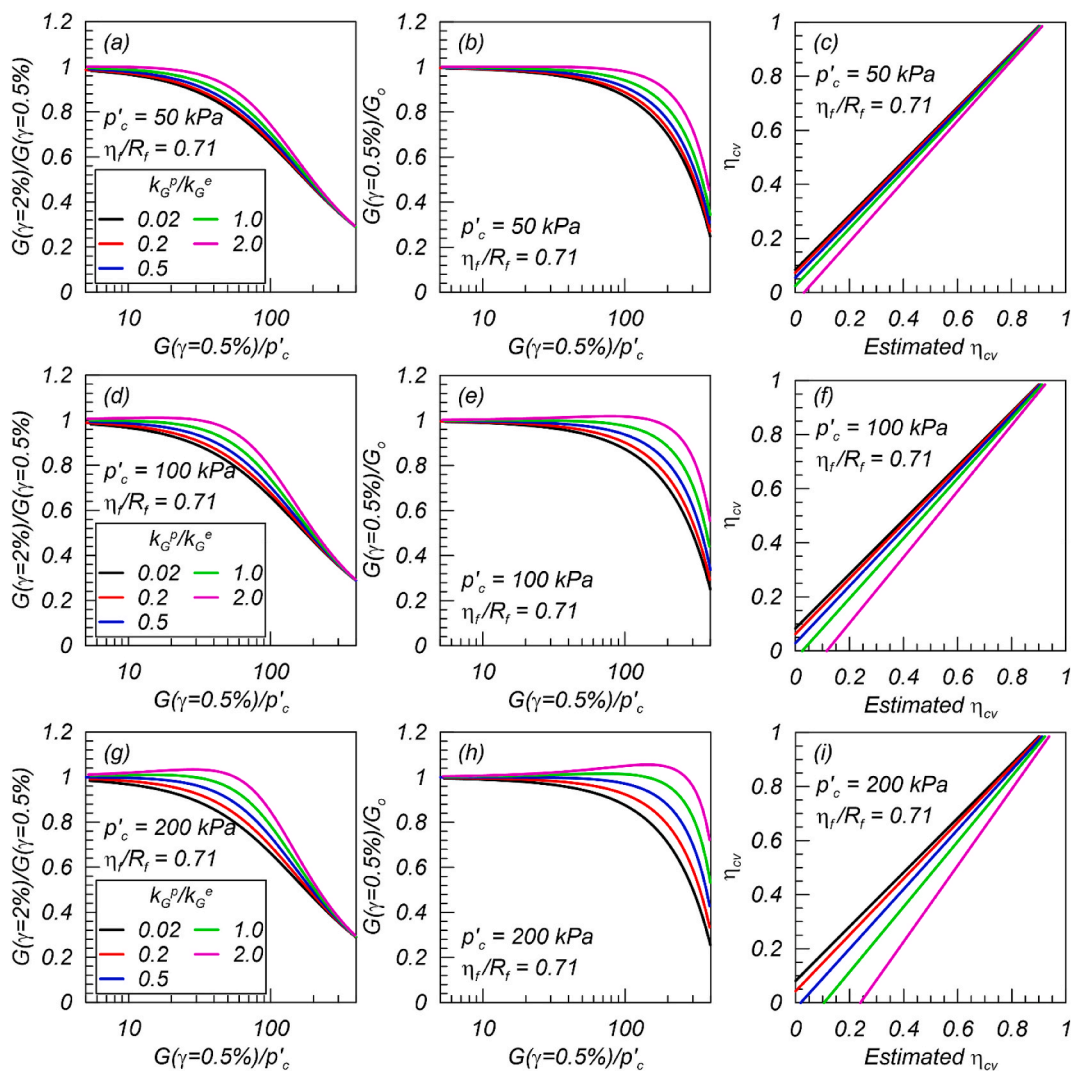
Fig. B4. Variations in normalized secant modulus and η_{cv} for different values of k_G^p/k_G^e. ($\eta_f/R_f = 0.71$).
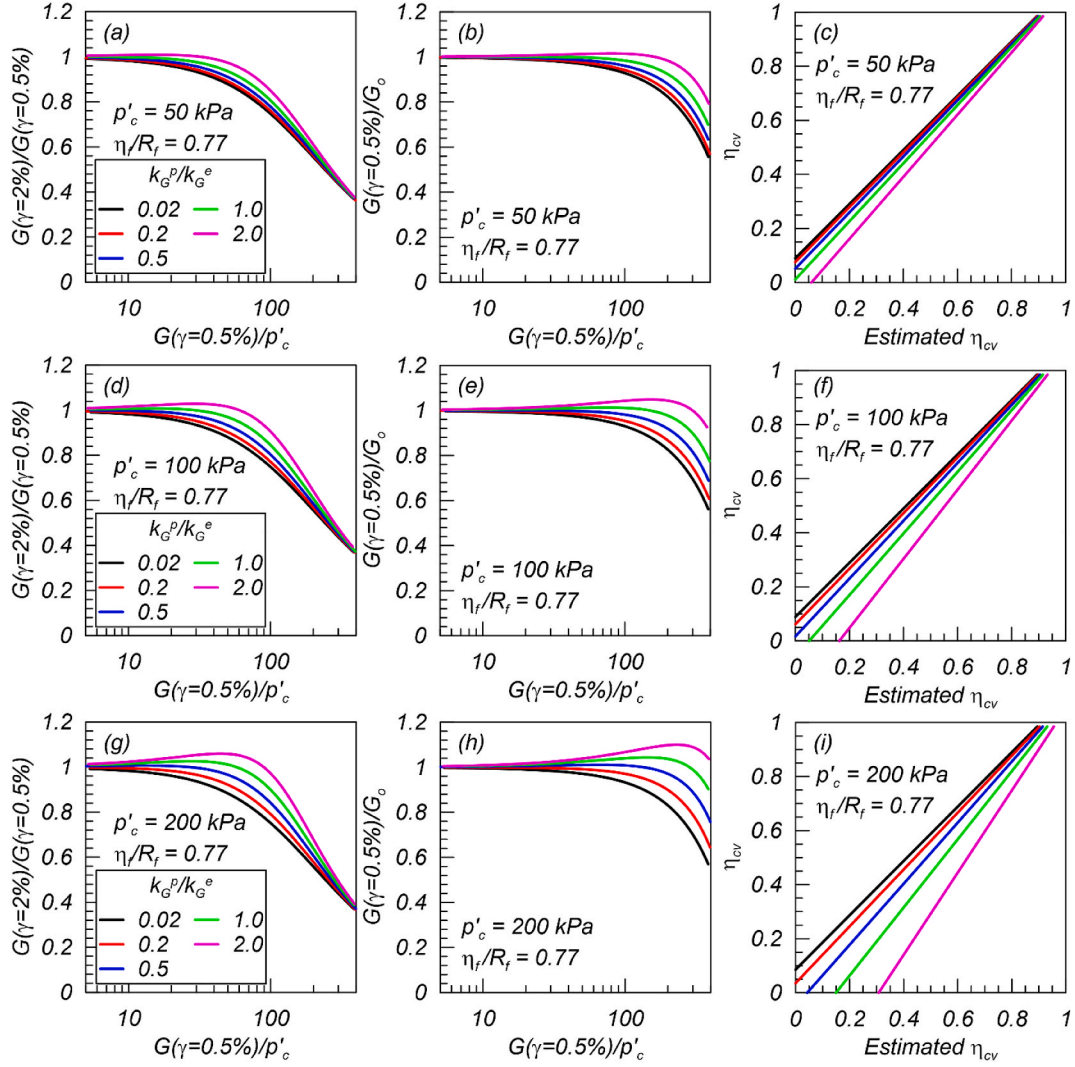
Fig. B5. Variations in normalized secant modulus and η_{cv} for different values of k_G^p/k_G^e. ($\eta_f/R_f = 0.77$).

APPENDIX C. Elastoplastic compliance & stiffness matrices

The four terms of the compliance matrix, in Eqs (10) and (11) can be written in terms of the model parameters upon substituting Eq. (7) into Eq. (11). The corresponding formulae are:

$$C_{11} = \frac{1}{k_G^p \left(\frac{p_M'}{p_a}\right)^{np}\left(1-\frac{\eta_{mob}}{\eta_f/R_f}\right)^2 p_M'}\left[\frac{3(1-2\nu)}{2(1+\nu)}\frac{k_G^p}{k_G^e}\left(\frac{p_M'}{p_a}\right)^{1+np-ne}\left(1-\frac{\eta_{mob}}{\eta_f/R_f}\right)^2 - \eta_{mob}(\eta_{cv}-\eta_{mob})\right] \tag{C1a}$$

$$C_{12} = \frac{1}{k_G^p \left(\frac{p_M'}{p_a}\right)^{np}\left(1-\frac{\eta_{mob}}{\eta_f/R_f}\right)^2 p_M'}\left[\frac{-(1-2\nu)}{2(1+\nu)}\frac{k_G^p}{k_G^e}\left(\frac{p_M'}{p_a}\right)^{1+np-ne}\left(1-\frac{\eta_{mob}}{\eta_f/R_f}\right)^2 + (\eta_{cv}-\eta_{mob})\right] \tag{C1b}$$

$$C_{21} = \frac{1}{k_G^p \left(\frac{p_M'}{p_a}\right)^{np}\left(1-\frac{\eta_{mob}}{\eta_f/R_f}\right)^2 p_M'}\left(-\eta_{mob}\right) \tag{C1c}$$

$$C_{22} = \frac{1}{k_G^p \left(\frac{p_M'}{p_a}\right)^{np}\left(1-\frac{\eta_{mob}}{\eta_f/R_f}\right)^2 p_M'}\left[\frac{k_G^p}{k_G^e}\left(\frac{p_M'}{p_a}\right)^{1+np-ne}\left(1-\frac{\eta_{mob}}{\eta_f/R_f}\right)^2 + 1\right] \tag{C1d}$$

The four terms of the stiffness matrix, in Eq (12) can be written in terms of the model parameters upon substituting Eqs. (1), (2) and (7) into Eq. (12). The corresponding formulae are:

$$D_{11} = \frac{1}{H^*} k_G^e p_a \left(\frac{p_M'}{p_a}\right)^{ne} \left[\frac{k_G^p}{k_G^e}\left(\frac{p_M'}{p_a}\right)^{1+np-ne}\left(1 - \frac{\eta_{mob}}{\eta_f/R_f}\right)^2 + 1\right] \tag{C2a}$$

$$D_{12} = \frac{1}{H^*} k_G^e p_a \left(\frac{p_M'}{p_a}\right)^{ne} \left[\frac{(1-2\nu)}{2(1+\nu)}\frac{k_G^p}{k_G^e}\left(\frac{p_M'}{p_a}\right)^{1+np-ne}\left(1 - \frac{\eta_{mob}}{\eta_f/R_f}\right)^2 - (\eta_{cv} - \eta_{mob})\right] \tag{C2b}$$

$$D_{21} = \frac{1}{H^*} k_G^e p_a \left(\frac{p_M'}{p_a}\right)^{ne} \eta_{mob} \tag{C2c}$$

$$D_{22} = \frac{1}{H^*} k_G^e p_a \left(\frac{p_M'}{p_a}\right)^{ne} \left[\frac{3(1-2\nu)}{2(1+\nu)}\frac{k_G^p}{k_G^e}\left(\frac{p_M'}{p_a}\right)^{1+np-ne}\left(1 - \frac{\eta_{mob}}{\eta_f/R_f}\right)^2 - \eta_{mob}(\eta_{cv} - \eta_{mob})\right] \tag{C2d}$$

where

$$H^* = \frac{3(1-2\nu)}{2(1+\nu)}\left[\frac{k_G^p}{k_G^e}\left(\frac{p_M'}{p_a}\right)^{1+np-ne}\left(1 - \frac{\eta_{mob}}{\eta_f/R_f}\right)^2 + 1 - \frac{\eta_{mob}}{3}\right] - \eta_{mob}(\eta_{cv} - \eta_{mob}) \tag{C2e}$$

APPENDIX D. Graphical illustration of Eqs. 24 and 25

Hypergeometric Functions (HF) are special forms of power series in one independent variable with a known general term a_n which, therefore, can be integrated and differentiated analytically. HF can also be viewed as solutions to linear differential equations of variable coefficients around a regular singular point, where the recursive relation defining the power series solution involves only two terms (say a_n and a_{n+l} where l is the step of the power series) which allows defining the general term of the series in closed form.

All differential equations associated with the special functions of mathematical physics (such as exponential, sinusoidal, power law, Bessel, Airy functions, Legendre polynomials, Chebyshev polynomials, elliptic integrals etc.) of real or complex argument are expressible in terms of hypergeometric functions. Since a hypergeometric function can represent any special function in mathematical physics, it is practically impossible to make a general statement about its behavior apart from all being invariably expressible in terms of power series with a known general term.

The function $_2F_1$ is the first hypergeometric function to be introduced (by Gauss in 1813) and is expressed in the general form

$$_2F_1(a,b,c,x) = \sum_{n=0}^{\infty} \frac{(a)_n\,(b)_n}{(c)_n}\frac{x^n}{n!} = 1 + \frac{a\,b}{c}\frac{x}{1!} + \frac{a(a+1)\,b(b+1)}{c(c+1)}\frac{x^2}{2!} + \ldots \tag{D-1}$$

where $(a)_n$, $(b)_n$, $(c)_n$ are parameters defined by means of the rising Pochhamer symbol

$$(q)_n = \begin{cases} 1, n = 0 \\ q(q+1)\ldots(q+n-1), n > 0 \end{cases} \tag{D-2}$$

and x is the independent variable.

The series naturally terminates if either a or b is a non-positive integer, which then reduces to a polynomial.

Because the coefficients governing coefficients a, b and c can attain any value (integer, rational, real or complex), the function itself could exhibit oscillatory or exponential-like behavior depending on the values of these parameters. Apart from that, little can be said about its properties and values except for certain special cases. Evidently, contrary to many functions of mathematical physics (notably Bessel functions) the behavior of which mostly unkown, the behavior of Hypergeometric functions is not well known even to experts in applied mathematics.

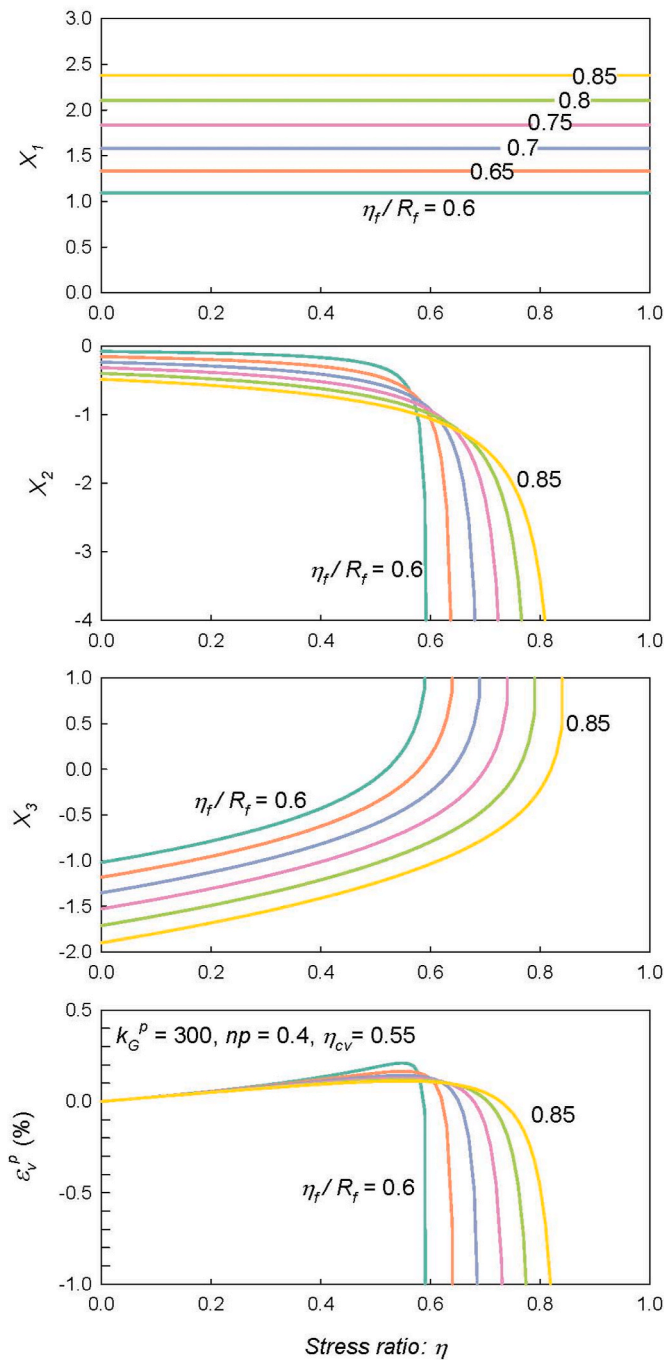The functions arising in this study exhibit the behavior shown in Figure D1 below.

Fig. D1. Plastic volumetric strain evaluated by the analytical solution in Eqs. 24 and 25 and graphical illustration of the terms X_1, X_2, X_3 of the equation involving hypergeometric functions.

References

[1] Beaty MH, Byrne PM. An effective stress model for predicting liquefaction behaviour of sand. Geotechnical Earthquake Engineering and Soil Dynamics III ASCE Geotechnical Special Publication 1998;75(1):766–77.

[2] Beaty MH, Byrne PM. UBCSAND constitutive model: version 904aR. *Documentation report: UBCSAND constitutive Model on Itasca UDM web site*. February 2011, http://www.itasca-udm.com/pages/UBCSand.html; 2011.

[3] Tsegaye A. PLAXIS liquefaction model. 2010. Report no. 1. PLAXIS knowledge base.

[4] Schofield AN, Wroth P. Critical state soil mechanics. McGraw-Hill Book Company; 1968.

[5] Prévost JH, Hoeg K. Effective stress-strain-strength model for soils. J. Geotech. Eng. ASCE 1975;101:259–78. GT3, Proc. Paper 11157.

[6] Nova R, Wood DM. A constitutive model for sand in triaxial compression. Int J Numer Anal Methods GeoMech 1979;3(3):255–78.

[7] Manzari MT, Dafalias YF. A critical state two-surface plasticity model for sands. Geotechnique 1997;47(2):255–72. https://doi.org/10.1680/geot.1997.47.2.255.

[8] Jefferies MG. Nor – sand: a simple critical state model for sand. Geotechnique 1993;43(1):91–103.

[9] Pestana JM, Whittle AJ. Compression model for cohesionless soils. Geotechnique 1995;45(4):611–31. https://doi.org/10.1680/geot.1995.45.4.611.

[10] Papadimitriou AG, Bouckovalas G. Plasticity model for sand under small and large cyclic strains: a multiaxial formulation. Soil Dynam Earthq Eng 2002;22(3):191–204. https://doi.org/10.1016/S0267-7261(02)00009-X.

[11] Been K, Jefferies MG. Stress-dilatancy in very loose sand. Can Geotech J 2004;41:972–89. https://doi.org/10.1139/T04-038.

[12] Loukidis D, Salgado R. Modeling sand response using two-surface plasticity. Comput Geotech 2009;36(1–2):166–86. https://doi.org/10.1016/j.compgeo.2008.02.009.

[13] Karamitros DK. Development of a numerica:l algorithm for the dynamic elastoplastic analysis of geotechnical structures in two and three dimensions. Athens: Dept of Civil Engineering, NTUA; 2010. PhD Thesis.

[14] Diambra A, Ibraim E, Russell AR, Wood DM. Fibre reinforced sands: from experiments to modelling and beyond. Int J Numer Anal Methods GeoMech 2013; 37(15):2427–55.

[15] Boulanger RW, Ziotopoulou K. PM4Sand (Version 3): a sand plasticity model for earthquake engineering applications. Report No. UCD/CGM-15/01. Center for Geotechnical Modeling Department of Civil and Environmental Engineering University of California Davis; 2015.

[16] Cubrinovski M, Ishihara K. State concept and modified elastoplasticity for sand modelling. Soils Found 1998;38(4):213–25.

[17] Hashiguchi K, Mase T, Yamakawa Y. Elaborated subloading surface model for accurate description of cyclic mobility in granular materials. Acta Geotechnica 2021;17:699–719. https://doi.org/10.1007/s11440-021-01203-y.

[18] Yang M, Seidalinov G, Taiebat M. Multidirectional cyclic shearing of clays and sands: evaluation of two bounding surface plasticity models. Soil Dynam Earthq Eng 2019;124:230–58.

[19] Barrero AR, Taiebat M, Dafalias YF. Modeling cyclic shearing of sands in the semifluidized state. Int J Numer Anal Methods GeoMech 2020;44:371–88.

[20] Yang M, Taiebat M, Dafalias YF. SANISAND-MSf: a sand plasticity model with memory surface and semifluidised state. Geotechnique 2020. https://doi.org/10.1680/jgeot.19.P.363.

[21] Duque J, Yang M, Fuentes W, Mas D, Taiebat M. Characteristic limitations of advanced plasticity and hypoplasticity models for cyclic loading of sands. Acta Geotechnica 2021. https://doi.org/10.1007/s11440-021-01418-z.

[22] Asaoka A, Noda T, Yamada E, Kaneda K, Nakano M. An elasto-plastic description of two distinct volume change mechanisms of soils. Soils Found 2002;42(5):47–57.

[23] Corti R, Diambra A, Wood DM, Escribano DE, Nash DFT. Memory surface hardening model for granular soils under repeated loading conditions. J Eng Mech 2016;142(12):04016102.

[24] Itasca. FLAC, fast Lagrangian analysis of continua. Version 7.0. Minneapolis, MN: Itasca Consulting Group; 2011. 2011, http://www.itascacg.com/.

[25] Shriro M, Bray JD. Calibration of numerical model for liquefaction-induced effects on levees and embankments, vol. 29. Chicago: Seventh International Conference on Case Histories in Geotechnical Engineering; 2013. April – 3 May.

[26] PLAXIS. Computer aided geotechnical analysis software. Bentley Systems; 2018. https://www.bentley.com/en/products/brands/plaxis.

[27] Puebla H, Byrne PM, Phillips R. Analysis of CANLEX liquefaction embankments: prototype and centrifuge models. Can Geotech J 1997;34:641–57.

[28] Petalas A, Galavi V. PLAXIS liquefaction model UBC3D-PLM. Available online: https://communities.bentley.com/cfs-file/_key/communityserver-wikis-components-files/00-00-00-05-58/UBC3D_2D00_PLM_2D00_REPORT.June2013.pdf. [Accessed 22 August 2022].

[29] Yimsiri S, Soga K. DEM analysis of soil fabric effects on behaviour of sand. Geotechnique 2010;60(6):483–95. https://doi.org/10.1680/geot.2010.60.6.483.

[30] Makra A. Evaluation of the UBC3D-PLM constitutive model for predictions of earthquake induced liquefaction on embankment dams. MSc Thesis. Delft University; 2013.

[31] Beaty MH. Application of UBCSAND to the LEAP centrifuge experiments. Soil Dynam Earthq Eng 2018;104:143–53.

[32] Anthi M, Gerolymos N. A calibration procedure for sand plasticity modeling in earthquake engineering: application to TA-GER, UBCSAND and PM4SAND.

Earthquake Geotechnical Engineering for Protection and Development of Environment and Constructions 2019. https://doi.org/10.1201/9780429031274. Francesco Silvestri, Nicola Moraci, CRC Press.

[33] Park S-S, Doan N-P, Nong Z. Numerical prediction of settlement due to the Pohang earthquake. Earthq Spectra 2020;37(2):652–85. https://doi.org/10.1177/8755293020957345.

[34] Chou J-C, Yang H-T, Lin D-G. Calibration of Finn model and UBCSAND model for simplified liquefaction analysis. *Procedures*. Appl Sci 2021;11:5283. https://doi.org/10.3390/app11115283.

[35] Li G, Liu Y-J, Dano C, Hicher P-Y. Grading-dependent behavior of granular materials: from discrete to continuous modeling. J. Eng. Mech. ASCE 2015;141(6):04014172.

[36] Lee KL, Seed HB. Drained strength characteristics of sands. J Soil Mech Found Div 1967;93(SM6):117–41.

[37] Seed and Idriss. Soil moduli and damping factors for dynamic response analyses. Report EERC70-10, earthquake engineering Research center. Berkeley: University of California; 1970.

[38] Hardin BO, Drnevich VP. Shear modulus and damping in soils: Design equations and curves. J. Soil Mech. Found Div. ASCE 1972:667–92.

[39] Bolton MD. The strength and dilatancy of sands. Geotechnique 1986;36(1):65–78. https://doi.org/10.1680/geot.1986.36.1.65.

[40] Darendeli MB. Development of a new family of normalized modulus reduction and material damping curves. The University of Texas at Austin; 2001. PhD Thesis.

[41] Duncan JM, Chang CY. Nonlinear analysis of stress and strain in soils. J. Soil Mech. Found Div. ASCE 1970;96(5):1629–53.

[42] Ishihara K. Liquefaction and flow failure during earthquakes. Geotechnique 1993; 43(3):351–451.

[43] Yamamuro J, Lade PV. Steady-state concepts and static liquefaction of silty sands. J Geotech Geoenviron Eng 1998;124(9):868–77.

[44] Hardin BO. The nature of stress-strain behaviour for soils. Pasadena: *Proceedings of Earthquake Engineering and Soil Dynamics, ASCE*; 1978. p. 3–89. 19-21 June 1978.

[45] Hoque E, Tatsuoka F. Anisotropy in elastic deformation of granular materials. Soils Found 1998;38(1):163–79.

[46] Suwal LP, Kuwano R. Statically and dynamically measured Poisson's ratio of granular soils on triaxial laboratory specimens. Geotech Test J 2018;36(4):493–505.

[47] Abramowitz M, Stegun I. *Handbook of mathematical Functions with formulas*. Graphs, and mathematical tables. Dover Publications; 1970. 0486612724.

[48] Global Cement. The growing cement industry of the UAE. https://www.globalcement.com/magazine/articles/917-the-growing-cement-industry-of-the-uae; 2015. November 2022.

[49] Emirates Steel. Emirates Steel signs slag management agreement with Finnish company ECOFER Technologies – emirates Steel. https://www.emiratessteelarkan.com/press/emirates-steel-signs-slag-management-agreement-with-finnish-company-ecofer-technologies/; 2022. November 2022.

[50] Krumbein WS, Sloss LL. Stratigraphy and sedimentation. second ed. San Franciscopp: W.H. Freeman and Company; 1963. p. 660.

[51] EN 13450. Aggregates for railway ballast. European Standard Norme Européenne Europäische Norm; 2013.

[52] Bishop AW. The strength of soils as engineering materials. Sixth rankine lecture. Geotechnique 1966;16:89–130. https://doi.org/10.1680/geot.1966.16.2.91.

[53] Vaid YP, Negussey D. A critical assessment of membrane penetration in the triaxial test. Geotech Test J 1984;7(2):70–6.

[54] Sun QD, Indraratna B, Nimbalkar S. Deformation and degradation mechanisms of railway ballast under high frequency cyclic loading. J Geotech Geoenviron Eng 2016;142(1):04015056.